Toward Tectonic-Type and Global 1D Seismic Models of the Upper Mantle Constrained by Broadband Surface Waves

Chiara Civiero, Sergei Lebedev, Yihe Xu, Raffaele Bonadio, François Lavoué

Toward tectonic-type and global 1D seismic models of the upper mantle constrained by broadband surface waves

Chiara Civiero[*1,2], Sergei Lebedev[2,3], Yihe Xu[2,3], Raffaele Bonadio[2,3], François Lavoué[2,4,5]

1) Department of Mathematics, Informatics and Geosciences, University of Trieste, Italy
2) Dublin Institute for Advanced Studies (DIAS), Dublin D02 Y006, Ireland
3) Bullard Laboratories, Department of Earth Sciences, University of Cambridge, Cambridge CB30EZ, UK
4) Institut de Radioprotection et Sûreté Nucléaire (IRSN), PSE-ENV, SCAN, BERSSIN, Fontenay-aux-Roses, France
5) Université Grenoble Alpes, Univ. Savoie Mont Blanc, CNRS, IRD, UGE, ISTerre, Grenoble, France

[*]Corresponding author (cciviero@icm.csic.es)

Accepted version for publication in the *Bulletin of the Seismological Society of America*

Key points:

1) Large surface-wave datasets constrain accurate global and tectonic-type average phase-velocity (C) models

2) Inversions of C yield Vs profiles with uncertainties, strongly dependent on their radial resolution

3) A flip in the sign of radial anisotropy from positive ($V_{SH} > V_{SV}$) to negative is observed at 200-300 km depth

Abstract

The unprecedentedly dense current sampling of the upper mantle with seismic data offers an opportunity for determining representative seismic velocity models for the Earth's main tectonic environments. Here, we use over 1.17 million Rayleigh and 300,000 Love-wave, fundamental-mode, phase-velocity curves, measured with multimode waveform inversion of data available since the 1990s, and compute phase-velocity maps in a 17-310 s period range. We then compute phase-velocity curves averaged over the globe and 8 tectonic environments and invert them for 1D seismic velocity profiles of the upper mantle. The averaged curves are smooth and fit by V_S models with very small misfits, under 0.1%, at most periods. For phase-velocity curves extending up to 310 s, Rayleigh waves resolve V_{SV} structure down to the shallow lower mantle. Love-wave sampling is shallower, and V_{SH} and, thus, radial anisotropy profiles are resolved down to 375-400 km depth. The uncertainty of the V_S models is dominated by the trade-offs of Vs at neighbouring depths. Using the model-space-projection approach, we quantify the uncertainty of Vs in layers of different thickness and at different depths and show how it decreases with the increasing thickness of the layers. Example 1D Vs models that fit the data display the expected increase of the lithospheric seismic velocity with the age of the oceanic lithosphere and with the average age of the continental tectonic type. Radial anisotropy in the global and most tectonic-type models show a flip of the sign from positive ($V_{SH} > V_{SV}$) to negative at 200-300 km depth. Negative anisotropy is also observed in the shallow mantle lithosphere beneath oceans, down to 45-55 km depth. We also compute a global model with minimal structural complexity, which fits the data worse than the best-fitting one but does not include a sub-lithospheric low-velocity zone, providing a simple reference for seismic studies.

1. Introduction

Radial changes in seismic velocities within the Earth depend on the rock composition, mineral phase transformations, and variations of elastic moduli with pressure and temperature (e.g., Anderson, 1999; Kennett and van der Hilst, 1998; Nolet et al., 1994). A range of one-dimensional (1D) reference seismic models have been built in the past to capture such radial changes. These models were created with different data sets, modelling approaches, and for different purposes, which resulted in substantial differences between them. The strong lateral heterogeneity of the lithosphere and underlying upper mantle is reflected in the large discrepancies between models computed for different locations and different tectonic environments. It is also responsible for the differences between global reference 1D models, which diverge depending on the amount and sensitivity of the data used to estimate them, and on how they were averaged over the globe.

Starting from the early 1950s, the crustal and upper mantle structure attracted an increasingly close attention of Earth scientists. Gutenberg (1953) used data from deep-focus earthquakes in Japan between 1930 and 1940 to calculate the P- and S-wave velocities in the mantle. Jeffreys and Bullen (1958) published travel-time tables for P, S, and core phases based on readings of natural earthquakes, and from those tables, the Jeffrey-Bullen (J-B) Earth model was derived. Lehmann (1961) constructed a 1D P- and S-wave velocity model that was based on body-wave travel times. The model has a low-velocity zone in the upper mantle and a sharp increase in P- and S-wave velocities at its lower boundary. Thereafter, other workers suggested that this Lehmann discontinuity (abbreviated as “L discontinuity” by Revenaugh and Jordan, 1991) occurs globally at an average depth of 220 km (Anderson, 1979; Hales, 1991). The Gutenberg, J-B, and Lehmann models were obtained mainly from continental data and thus biased towards continents. New travel-time tables of P waves were derived by Herrin (1968) from more accurate data from earthquakes and underground nuclear explosions.

Advances in instrumentation and computational resources in the 1970-1980s made it possible to construct increasingly accurate models, constrained by larger datasets of different data types. Dziewonski and Anderson (1981) computed the Preliminary Reference Earth Model (PREM) model, using free oscillation data, surface-wave dispersion curves and the P- and S-wave travel times collected by the International Seismological Centre (ISC). In addition, the

model was constrained to fit the Earth's mass and moment of inertia. PREM provides V_P, V_S, density, anelasticity, and radially anisotropic structure for both P- and S-wave velocities and shows a discontinuity at 220 km depth, as well as the 400 and 670 km discontinuities bounding the mantle transition zone (MTZ). Through a probabilistic approach, Beghein et al. (2006) recomputed PREM using normal-mode and surface-wave phase-velocity data in a wide frequency range. A revised version of PREM has also been proposed also by Kustowski et al. (2008). Their 1D transversely isotropic reference model, called STW105, was computed as a spherical average of their 3D anisotropic model using surface wave-phase anomalies, long-period waveforms, and body wave travel times. STW105 provides radial profiles for density, and seismic velocities V_P and V_S.

Kennett and Engdahl (1991) derived their IASP91 model using P- and S-wave travel-time data up to 1987. For the refined AK135 model (Kennett et al., 1995), the P-wave data were extended to 1991. AK135 was constructed as a reference model for travel-time data to be used, in particular, for earthquake location and seismic phase identifications. This model was derived from fitting ISC travel-time data and included isotropic P- and S-wave velocity profiles. AK135 differs from IASP91 only for the reduced velocity gradients at the inner core boundary.

Another model derived from body-wave travel times reported in the ISC Bulletins is SP6 (Morelli and Dziewonski, 1993). It comprises P- and S-wave velocity profiles constrained by these data, and it is similar to the IASP91 and AK135 models but is based on a different philosophy. Whereas IASP91 and AK135 were computed for optimal determination of earthquake locations, SP6 was aimed at the construction of a global average model. Similarly to the early Gutenberg, J-B and Lehmann models, IASP91 and AK135 are likely biased towards continents, and the SP6 model was specifically corrected to reduce this bias.

In addition to the global 1D models, a number of widely used continental and oceanic-scale profiles have been produced over the last 60 years. At continental scale, Brune and Dorman (1963) computed a layered V_S model of the crust and upper mantle beneath the Canadian Shield using Rayleigh and Love phase velocities combined with travel-time data. This study does not show the L discontinuity to occur in normal continental regions around 200 km. Other two widely used 1D velocity profiles for the tectonically active and cratonic areas of North America (tectonic North America ‘TNA’ and stable North America ‘SNA’,

121 respectively) were computed by Grand and Helmberger (1984) using the waveforms and
122 travel times of S and SS phases, sampling down to the depth of 900 km. The models show
123 significant S-wave velocity differences down to 350 km depth, with the velocities of SNA
124 substantially higher than those of TNA. Based on inversion of long-period surface-wave,
125 body-wave, and ScS reverberation data, Gaherty and Jordan (1995) computed the radially
126 anisotropic 1D model (AU3) for the upper mantle beneath stable continental Australia and
127 western Pacific. AU3 is characterized by an anisotropic mantle above an L discontinuity
128 located at a depth of around 252 km and an isotropic mantle below and by small jumps of
129 density, V_P, and V_S across the same discontinuity.
130
131 In oceans, shear velocity and anisotropy inversions of surface-wave phase velocities for paths
132 that traversed the Pacific show a progressive increase in velocity as a function of the age of
133 the seafloor down to a depth of about 200 km (Nishimura and Forsyth, 1989, 1988). The
134 velocity minimum and its depth increase with the seafloor age. Oceanic shear-speed profiles
135 (Dalton et al., 2009) also display a correlation between seafloor age and upper-mantle
136 attenuation, consistent with laboratory and geodynamic models, relating experimental shear
137 modulus and attenuation data to temperature and grain size variations (Dannberg et al., 2017;
138 Faul and Jackson, 2005).
139
140 Global, regional, and tectonic-type seismic-velocity models of the upper mantle are routinely
141 used in geophysical studies, both as reference in seismic imaging work and as representations
142 of the physical structure of the Earth. Broadly, they can comprise both reference phase-
143 velocity curves of Rayleigh and Love surface waves and the 1D V_S and V_P profiles. Regional
144 and tectonic-type models show large differences from the global reference ones and from one
145 another due to substantial lateral variations in the Earth's seismic velocity structure.
146
147 The first purpose of this study is to derive accurate average phase-velocity models for the
148 Earth's main tectonic environments from the very large available datasets. The sampling of
149 all tectonic types is currently very dense, and the resolution of seismic imaging is sufficiently
150 high for tectonic units to be distinguished from one another along their boundaries. Secondly,
151 we appraise the inversion of the data for 1D seismic velocity profiles, with particular
152 attention to the data sensitivity and the model uncertainty. Example profiles of shear-wave
153 velocities and their radial anisotropy illustrate the basic properties of the lithosphere of
154 different ages in the oceans and of different ages, composition, and evolution in the

155 continents. Although the seismic-velocity models do not amount to complete physical models
156 of the Earth such as PREM, they can pave the way for a new generation of such models by
157 providing accurate phase-velocity data for the Earth's different tectonic environments.
158 Specifically, these phase-velocity models can be inverted, possibly together with other
159 geophysical and geological data, for multi-parameter physical models (e.g., Cammarano et
160 al., 2005; Fullea et al., 2021), including temperature, composition, density, etc. beneath the
161 Earth's main tectonic environments.
162
163 We use a massive dataset of phase-velocity measurements of Rayleigh and Love fundamental
164 modes, obtained with multimode waveform inversion using virtually all available broadband
165 data since the 1990s. We analyse the depth sensitivity of the surface-wave data and determine
166 the dependence of the maximum depths of the sensitivity and resolution on the period range
167 of the phase-velocity measurements for the vertically and horizontally polarised shear-wave
168 speeds and for radial anisotropy. We then use our very large global dataset to calculate
169 average Rayleigh and Love phase-velocity curves for the globe and for eight primary
170 tectonic-type environments on Earth, which we map using tomography-based tectonic
171 regionalisation. Inverting these broadband phase-velocity curves, we compute new 1D
172 average seismic models for the globe and for the considered tectonic environments and
173 analyse their uncertainty and its variation with the radial averaging length, as well as with
174 depth. We also discuss some immediate inferences from the new models regarding the
175 variations in the lithospheric structure between different tectonic environments and the cross-
176 tectonic-type variations in radial anisotropy.
177
178 **2. Data and method**
179
180 Surface-wave phase velocities are highly sensitive to the shear-wave velocity within the crust
181 and upper mantle. The fundamental mode of Rayleigh or Love surface waves is usually the
182 most energetic arrival on the vertical- or transverse-component seismogram, respectively.
183 The surface-wave propagation is dispersive in nature, sampling greater depths with
184 increasing wavelengths. Surface waves at short periods are then more sensitive to the crustal
185 structure, and long periods are sensitive to depths down to the base of the upper mantle
186 (Figure 1). Variations in surface-wave dispersion measured along different source-station
187 paths provide a direct indication of the structure within the Earth, and measurements at
188 different periods can constrain heterogeneity at different depths.

189
190 **2.1. Depth sensitivity of the fundamental mode surface waves**
191
192 Shear-speed models derived from Rayleigh-wave dispersion represent vertically polarized
193 shear waves (V_{SV}) while those constrained by Love-wave dispersion correspond to
194 horizontally polarized waves (V_{SH}). In order to assess the sensitivity of phase-velocity curves
195 to shear-wave velocities at depth we perform a series of specially designed tests. For the
196 purposes of the inversion, we use the arithmetic isotropic shear-velocity average:

$$\boldsymbol{Vs} = \frac{\boldsymbol{V_{SV} + V_{SH}}}{\mathbf{2}}, \quad (1)$$

197 with the radial anisotropy defined as:

$$R = \frac{V_{SH} - V_{SV}}{Vs}, \quad (2)$$

198
199 where V_{SV} and V_{SH} are the vertically and horizontally polarized shear speeds, respectively.
200 We assume an isotropic shear-velocity model with minimum complexity, with constant V_S
201 from the Moho to 200 km depth and with V_S increasing below, similar to most reference
202 models (black dashed line in Figure 2), and compute Love and Rayleigh phase-velocity
203 curves for this model. These curves are then inverted using a strong regularisation that pushes
204 V_{SH} and V_{SV} values towards *a priori* +250 m/s anomalies and, in other tests, towards –250
205 m/s anomalies throughout the mantle. Where the phase-velocity data has a strong sensitivity
206 to the structure, the model produced by the inversion will stay close to the 'true' model,
207 despite the regularisation pulling it away from that. At depths where there is no data
208 sensitivity, the model will deviate from the true one by as much as it is encouraged to do so
209 by the regularisation.
210
211 The results of this series of tests show how the maximum depth of the sensitivity depends on
212 the maximum period of the data (Figure 2). We distinguish the depth limit of substantial
213 sensitivity, where, despite the strong regularisation, the output model stays much closer to the
214 true model than to the regularisation-suggested one, and the depth limit of resolution, where
215 the sensitivity is strong and sufficient to resolve depth variations and amplitudes of
216 anomalies. The substantial sensitivity depth limit is estimated as the depth where the V_S
217 deviation from the true value does not exceed 0.05 km/s, and the resolution depth limit where
218 the deviation does not exceed 0.02 km/s. We repeat the test inversions with the synthetic data
219 with different period ranges, spanning from a constant minimum period of 17 s (for Rayleigh

waves) and 24 s (for Love waves) to a maximum period that is varied (100, 150, 200, 250 and 300 s).

At periods up to 100 s, the sensitivity and resolution depths are similar for V_{SV} and V_{SH}, constrained by Rayleigh and Love phase velocities, respectively (resolution depth limits of 200 and 190 km, respectively). At longer periods, the depth sensitivity of Rayleigh waves exceeds that of Love waves. The Rayleigh phase-velocity curve with a 300 s maximum period is sensitive to V_{SV} at depths well into the lower mantle and can resolve V_{SV} structure down to the bottom of the MTZ. Love-wave phase-velocity data with a 300-s maximum period, by contrast, shows substantial sensitivity to V_{SH} down to 410 km depth only and is likely to resolve structure accurately down to 370 km.

Radial anisotropy is defined by the difference between V_{SV} and V_{SH} (where positive anisotropy is $V_{SH} > V_{SV}$), and the greatest depth it can be resolved is determined by the V_{SH} resolution depth limit, which is the smallest of the two. Isotropic-average V_S resolution depth limit will, generally, vary between the V_{SV} and V_{SH} resolution depth limits, depending on the anisotropy profile. Where radial anisotropy in the deep upper mantle is strong, isotropic average V_S will be resolved accurately only up to the depth where V_{SH} is resolved accurately. Where the anisotropy is weak and, in particular, is much smaller than the anomalies in V_{SV} and V_{SH}, isotropic-average V_S can be resolved with useful accuracy at depths close to the resolution limit of V_{SV}.

The phase-velocity curves used in this study extend up to 310 s periods. According to the sensitivity testing (Figure 2), the data can resolve V_{SV} structure down to the bottom of the MTZ and V_{SH} and radial anisotropy down to the top of the MTZ. Our results (Section 3) show that seismic velocities in the MTZ vary between different environments by substantially more than the values of radial anisotropy in the 300-400 km depth range. If we can assume that the amplitudes of radial anisotropy in the MTZ and in the 300-400 km depth range are similar (Lavoué et al., 2021; Visser et al., 2008), then our isotropic average V_S profiles provide useful accuracy down to the bottom of the MTZ.

2.2. Phase-velocity measurements

In this work, we use a dataset of over 1.17 million Rayleigh- and 300,000 Love-wave fundamental-mode phase-velocity curves, across a broad period range of 10-460 s. The curves were obtained by the Automated Multimode Inversion (AMI, Lebedev et al., 2005) of waveforms of earthquake recordings, from 6,242 stations and 25,496 events worldwide. Earthquakes from the Global CMT catalogue (Dziewonski et al., 1981; Ekström et al., 2012) since 1994 were used, with source-receiver distances between 500 and 18,000 km and with magnitudes above a distance-dependent threshold (Lebedev and Van Der Hilst, 2008; Schaeffer and Lebedev, 2013). Some data were also selected from the early 1990s (Lebedev and Van Der Hilst, 2008). AMI extracts information on P- and S-wave velocity variations by non-linear fitting of time-domain teleseismic waveforms. This information was used to obtain a number of recent 3D S-wave tomographic models (e.g., Celli et al., 2021, 2020; Chagas De Melo et al., 2022; De Laat et al., 2023; Lavoué et al., 2021; Schaeffer and Lebedev, 2014). As a by-product of the time-domain waveform fitting, AMI measures phase velocities for all modes that contribute significantly to each waveform fit. The interference of the fundamental-mode Rayleigh and Love waves with higher modes (e.g., Foster et al., 2014; Hariharan et al., 2020; Nettles and Dziewoński, 2011), which make up S and multiple S waves, is modelled as part of the multimode waveform inversion and, thus, fully taken into account, so that it does not affect the accuracy of the phase-velocity measurements. The low misfit thresholds and anti-cycle-skip precautions taken by AMI ensure that errors in the measurement of the phase of the signal are negligible. The main sources of errors come from the uncertainties in the hypocentre locations and origin times of the events, as well as the unaccounted-for fundamental-mode diffraction (e.g., Legendre et al., 2012). The dataset provides dense, broadband data coverage of the entire globe. The recent work of Moulik et al. (2021) demonstrates that the ray coverage of our fundamental-mode Rayleigh waves' collection is one of the highest among different datasets (Beucler and Montagner, 2006; Debayle and Ricard, 2012; Ekström, 2011; Ma et al., 2014; Ritsema et al., 2011; Yoshizawa and Kennett, 2002), with global average of hit counts for these waves greater than 3000. Our dataset provides finely sampled dispersion curves resulting in a very large number of data. The highest-frequency phase-velocity measurements tend to come from shorter paths, whereas the lowest-frequency measurements are from long paths. In this study, we invert only the fundamental-mode data, leaving the inversion of higher modes for future work. The fundamental-mode measurements are more numerous and yield global phase-velocity maps with higher lateral resolution than higher-mode potentially could (Masters et al., 1982),

286 which is important for accurately sampling and separating the areas of different lithospheric
287 types and ages.
288
289 **2.3. Phase-velocity tomography**
290
291 We invert the Rayleigh- and Love-wave fundamental-mode measurements for phase-velocity
292 maps at different periods. In order to obtain a dense sampling of the frequency range of the
293 measurements, we compute maps at 98 different periods, with a logarithmic sampling
294 interval increasing with the period (Agius and Lebedev, 2014). At each period, all phase-
295 velocity measurements are inverted together in a large linear system (Zhang et al., 2009,
296 2007) for the 2D distribution of Rayleigh- and Love-wave phase velocity and its 2ψ and 4ψ
297 azimuthal anisotropy, respectively. Each map is parametrized on a triangular grid (Wang and
298 Dahlen, 1995) with an average 200-km interknot spacing. The reference velocity of each map
299 is the average over all the phase-velocity measurements at the considered period. In order to
300 ensure regularisation consistency across different periods, we vary the regularisation
301 coefficients on each phase-velocity map by taking into account the different data sampling.
302 Figure 3 shows examples of Rayleigh- and Love-wave phase-velocity maps at different
303 periods (25, 50, 100, and 250 s for Rayleigh and 35, 50, 100 and 250 s for Love waves).
304
305 In order to minimize the impact of errors in the measurements on phase-velocity maps, we
306 exploit the data redundancy of the dataset and select only the most mutually consistent data
307 through an *a posteriori* outlier rejection procedure. At every period, we use the first-iteration
308 phase-velocity map to compute synthetic data by multiplying the sensitivity matrix and the
309 model vector. We then compare the synthetic and real data and discard the measurements
310 with the largest misfits. In our study, we keep thus-selected, most-mutually-consistent 70% of
311 the initial dataset and compute the final phase-velocity maps with these "de-noised" data.
312
313 **2.4. Local and average phase-velocity curves**
314
315 Our set of phase-velocity maps yields a total of 16,380 Rayleigh and Love phase-velocity
316 curve pairs (Figure 4), with one pair at each knot of our 2°-spaced global grid. We now
317 extract the dispersion curves point by point from the phase-velocity maps and split them
318 according to the tectonic environment they belong to, using a tomography-based tectonic
319 regionalisation of the Earth.

In this study, we refine the tectonic regionalisation by Schaeffer and Lebedev (2013), which used their SL2013sv tomographic model and the cluster analysis method, applied previously to tomography-base regionalisation by Lekic and Romanowicz (2011). We resample the tomographic model on a finer lateral grid than the original one, with 1D shear-speed profiles every 10 km and with a depth range between 30 and 350 km, to avoid spatial aliasing. The clustering analysis is carried out using the MATLAB implementation of the *k-means* algorithm. We refer to Schaeffer and Lebedev (2015) for the details of the *k-means* analysis. The 6 sets into which the shear-speed profiles were partitioned naturally distinguish the oceanic and continental lithospheres and the different types of each. The tectonically meaningful types of environments come out naturally and can be identified as: i) Archean cratons, ii) stable platforms, iii) Phanerozoic continents; iv) old-age oceans, v) intermediate-age oceans, and vi) ridges, backarcs and rifts (Schaeffer and Lebedev, 2015). In order to capture the differences in seismic velocities and anisotropy within the different tectonic environments of region vi), we further manually divide it into three geologically different lithospheric sub-types: rifts and continental hotspots; young oceans and ridges; backarcs (Figure 5).

We then compute the average Rayleigh and Love phase-velocity curves for the globe (Figure 4) and for each tectonic environment (Figure 6). The averaging of hundreds of point-by-point curves produces robust average phase-velocity curves for each region. Most of the measurements at the shortest periods are obtained from shorter paths, distributed unevenly. As a result, global maps at periods shorter than 17 s for Rayleigh and 23 s for Love show gaps in the data coverage. The greater phase-velocity variability at short periods relative to long periods reflects the greater lateral heterogeneity in the crust (e.g., Ekström et al., 1997; Laske, 1995). For periods greater than 17 and 23 s for Rayleigh and Love waves, respectively, phase-velocity measurements are available along paths that are more numerous, have a broader range of source-station distances, and are distributed more evenly, resulting in a complete global coverage. The source-station path coverage –and, thus, the resolution– decreases at periods greater than 310 s. The shortest- and longest-period tails of the dispersion curves are thus removed, to avoid biases. The final Rayleigh and Love-wave average curves span the period range of 17-310 s and 23-310 s, respectively.

353 The phase-velocity maps are a result of the inversions of the phase-velocity measurements,
354 and the phase-velocity curves we use in this work are averaged over regions of the maps. It is
355 not possible to relate the errors on these average dispersion curves to the estimated errors of
356 original, source-station, phase-velocity measurements that go into the phase velocity maps.
357 Errors of those original measurements were dealt with in a statistical manner by identifying
358 and removing the least mutually consistent data (Section 2.3). The remaining errors manifest
359 in frequency dependent noise in the phase-velocity maps.
360
361 The cratons' average dispersion curves do not differ substantially from the stable platforms
362 and Phanerozoic continents' ones at the periods that sample primarily the crust (<25 s) but
363 are faster than all the other continental curves at intermediate and long periods (Figure 7A)
364 due to their thick, cold, high-velocity mantle lithosphere. Rifts and continental hotspots show
365 the lowest average velocity at periods > 60 s. Rifts show the highest velocities at short
366 periods due to their thin crust relative to the other continental regions. Among oceanic
367 regions, backarcs display the lowest velocities at intermediate periods, followed by young
368 oceans, intermediate oceans, and old oceans (Figure 7B).
369
370 **2.5. Inversion for 1D shear-velocity models and radial anisotropy**
371
372 The global and tectonic-type average Rayleigh- and Love-wave dispersion curves can be
373 inverted for 1D profiles of the arithmetic-isotropic average shear-wave speed V_S and radial
374 anisotropy (Bonadio et al., 2021; Endrun et al., 2008; Lebedev et al., 2006). The Voigt
375 average or a quadratic definition of radial anisotropy can be calculated from the resulting V_S
376 and R if desired. To obtain radial anisotropy and isolate the isotropic-average seismic
377 velocity relatable to the temperature and composition of the rock at depth, the Rayleigh and
378 Love dispersion curves have to be inverted simultaneously (e.g., Anderson, 1961; Fullea et
379 al., 2012; Lebedev et al., 2006; Montagner, 2007).
380
381 The inversion is performed using a fully non-linear, Levenberg-Marquardt gradient search
382 (Lebedev et al., 2006; Meier et al., 2004). The search direction is computed at each iteration
383 with the Rayleigh- and Love-wave synthetic phase velocities calculated directly from the
384 anisotropic V_S model using a fast, streamlined version of the MINEOS modes code (Agius
385 and Lebedev, 2013; Nolet, 2008; Ravenna and Lebedev, 2018). The non-linear inversion
386 algorithm minimizes the synthetic-data misfit and converges to a best-fitting solution, with no

linearization of the forward problem. Compressional velocity V_P has a small but non-negligible influence on the phase velocity. Perturbations in V_P are assumed isotropic and coupled to the perturbations in isotropic-average shear velocity as δV_P (m/s) ≡ δV_S (m/s). They are not shown here for brevity. Perturbations are controlled by basis functions, in the shape of boxcars in the crust and triangles in the mantle down to the uppermost lower mantle, with denser sampling at shallower mantle depths (Agius and Lebedev, 2014; Bartzsch et al., 2011; Zhang et al., 2009). These functions sample the sensitivity depth range of the inversion parameters, V_S and radial anisotropy. The 410- and 660-km MTZ discontinuities are parameterised using pairs of half triangles, one above the discontinuity and the other below. The depth of the Moho and the crustal layer discontinuities are additional inversion parameters. Slight norm damping and vertical gradient damping were applied to both the isotropic V_S and to radial anisotropy parameters, with the regularisation parameters chosen empirically so as to discourage highly oscillatory, physically unrealistic models resulting from fitting noise but not to affect the amplitude of the structure required by the data. All the V_S models are perturbed from the surface to the topmost lower mantle (~1000 km depth), with the surface topography taken into account.

3. Results

3.1. Phase-velocity maps

The set of Rayleigh- and Love-wave phase-velocity maps samples the entire Earth's surface. The distribution of the phase velocities is smooth and continuous, both laterally and across most periods, with periods of 50-100 s sampled by the largest number of paths (Figure 3). Only for periods shorter than 20 s for Rayleigh and 30 s for Love, some gaps in the path coverage are present, especially in the oceans and in the African continent. Thanks to the large dataset and dense global coverage, we can resolve features on a finer scale than previous global phase-velocity maps and in a much broader period range than in previous studies (Dalton and Ekström, 2006; Durand et al., 2015; Ekström, 2011; Trampert and Woodhouse, 1995). For example, features like the strong low-velocity anomalies close to Iceland and beneath the Afro-Arabian rift system show very clear geometries that match recent tomographic images (Celli et al., 2021; Civiero et al., 2022). In West Africa and Australia, our maps resolve separate high-velocity cratonic cores where previous results

showed smoother units, highlighting the gain in the resolving power of our inversions, using new data.

At short periods (~20-30 s), the maps show high velocities in the ocean basins, as expected for the oceanic lithosphere (Figure 3). In the continents, thicker crust is reflected in lower phase velocities, and the lowest ones occur in major orogenic belts including the American Cordillera, Andes, Zagros, and Tibet, where the crust is particularly thick.

At intermediate periods (50-150 s), the fundamental-mode Rayleigh waves sample mostly the lithosphere in the thickest-lithosphere continents and both lithosphere and asthenosphere elsewhere (Figure 1). North-Eastern North America, Western Australia, Eastern Siberia, Eastern Europe, the São Francisco and Congo Cratons stand out with strong high-velocity anomalies. Below the mid-ocean ridges, the maps show low-velocity anomalies, with the lowest velocities under the fast-spreading centres, in particular the East Pacific Rise. Hotspots, rift regions and backarc basins also display pronounced low velocities, especially below Iceland, the East Africa-Arabia rift system, and Southeast Asia.

Longest-period surface-wave sensitivity spans from the base of the lithosphere down to the MTZ (Figures 1 and 2). This broad sensitivity-depth range makes the visual interpretation of the phase-velocity maps less intuitive compared to shorter period maps. For example, the signal of V_S anomalies within subducting slabs is averaged together with that from the depth ranges directly above and below them. At periods 200-300 s, we still observe prominent low-phase-velocity anomaly below the East African Rift, probably due to the hot mantle plume material rising beneath this region (Bastow et al., 2008; Boyce et al., 2021; Civiero et al., 2019, 2015), which propagates laterally from Afar to Tanzania (Civiero et al., 2022). Low velocities are also seen below south-western North America where a spreading centre appears to have been subducted recently (Zhang et al., 2014). Strong high-phase-velocity anomalies are seen in the Love-wave maps across cratonic Western Australia, Western Africa, North-eastern America, and Siberia.

3.2. Computing a global-average shear-velocity profile

In order to find profiles that fit both the surface-wave data and other available data, existing information on the crustal thickness, structure, velocity and density was included in the

452 background models. We average the values of the discontinuity depth, V_P, V_S, and density ρ
453 for each crustal layer in the global model of Earth's crust CRUST1.0 (Laske et al., 2013) and
454 insert these parameters in the background model. The Moho discontinuity depth is fixed
455 during this inversion. The average values are shown in Supplementary Table T1. In the
456 mantle, the background model is a modified version of AK135 (Kennett et al. 1995),
457 recomputed at 50 s and characterized by constant shear velocities of 4.45 km s^{-1} from the
458 Moho down to ~200 km depth and linearly increasing shear velocities below. The reference
459 period of the model is 50 s, approximately in the middle of the period range of the data, in the
460 logarithmic sense. This minimizes errors from uncertainties in the attenuation structure of the
461 mantle (Lebedev and Van Der Hilst, 2008) as shorter-period surface waves (20–50 s) sample
462 the largest variations in Q, including sharp Q decreases beneath mid-ocean ridges and
463 backarc basins due to the partial melting there (Forsyth et al., 2008). Density and the
464 compressional and shear attenuation factors are fixed at the reference values, taken from
465 PREM (Dziewonski & Anderson 1981) and AK135 (Kennett et al. 1995), respectively. The
466 eta parameter is assumed to be 1.
467
468 We now use the average Rayleigh and Love dispersion curves for the globe and eight tectonic
469 environments to solve for 1D depth-dependent profiles of V_S and R that are representative
470 examples of the models within the uncertainties (Section 4.3). The 1D models yielded by the
471 inversions are non-unique, as a range of different models can fit the data almost equally well.
472 A global 1D V_S model is shown in Figure 8, and the same model is plotted in Supplementary
473 Figure S1 on top of the density distribution of the 1D shear-speed profiles extracted from the
474 global tomographic model SL2013sv of Schaeffer and Lebedev (2013).
475
476 The dispersion curves that constrain the model are very smooth, indicating very small
477 random errors. We re-iterate that the phase-velocity maps at different periods are obtained in
478 inversions independent from one another. The phase-velocity curve at each point is
479 constructed using values at this point from all the 98 maps. There are errors in these maps,
480 they are frequency-dependent and, because each map is computed independently from all the
481 other ones, these cause roughness on the point-by-point phase-velocity curves. The errors are
482 reduced greatly by averaging over the numerous points across each tectonic environment,
483 which the smoothness of the curves confirms. The remaining errors can be seen in the
484 oscillations of the misfits with period but are well below 0.1% almost everywhere.
485

The total misfit is the sum of those for the Love and Rayleigh dispersion curves. In this inversion and in the following, we express the relative surface-wave misfit as the synthetic minus observed Rayleigh- and Love-wave phase velocities, divided by the observed phase velocities. Here, the model fits the data closely despite the global dispersion curves averaging over different tectonic environments. The misfit is very low, less than 0.1% at all periods for both types of surface waves. The largest misfit is at the shorter periods where sampling the greatest heterogeneity in the crust and uppermost mantle and is primarily due to the non-linearity of the relationship between the surface-wave phase velocities and the shear and compressional velocities at depth.

Beneath a 1.4-km deep-water layer, the model comprises a 4.5-km thick upper crust with relatively low velocities in it, a higher-velocity, 13-km thick middle crust, and a higher-velocity lower crust down to 23 km depth. A zoom on the V_S in the first 50 km depth is shown in Supplementary Figure S2. In the uppermost ~100 km of the mantle, the data require relatively high isotropic-average shear velocities, up to 4.5 km/s (Figure 8). Between 150 km depth and the top of the MTZ, shear speeds are close to AK135 while within the MTZ they are slightly lower. Compared to PREM, the isotropic V_S is higher in the shallowest upper mantle and in the MTZ.

The observed Rayleigh-wave average dispersion curve is close to that of PREM in its entire period range. The Love-wave average phase-velocity curve, by contrast, is noticeably faster than that predicted by PREM (Figure 8aiii). The Love-Rayleigh discrepancy (McEvilly, 1964) has long been attributed to radial anisotropy (Anderson, 1961). Radial anisotropy required by our global dataset is greater than that in the PREM model. Unlike in PREM, anisotropy is present in all the crustal layers in our model (Supplementary Figure S2). Between the Moho and 250 km depth, it is strongly positive, with values reaching 3% (Figure 8). By contrast, below ~300 km depth, slightly negative anisotropy (0.5-1.0%) is required by the data, down to the bottom of our model. This is a robust feature present in all models that fit these data.

To verify that the negative deep anisotropy is required by the data, we perform a test inversion, in which we constrain the radial anisotropy at depths greater than ~250 km to be zero, whereas all the other parameters are allowed to vary freely (Figure 9). We observe that if we prohibit the anisotropy to be negative in the deeper asthenosphere, the misfit

deteriorates at long periods (T > 150 s). This indicates that an isotropic upper mantle below 250 km would be inconsistent with the data and negative radial anisotropy ($V_{SV} > V_{SH}$) is required. The inferences from this observation are discussed in Section 4.

3.3. Tectonic-type shear-velocity profiles

Inversions for representative 1D radially anisotropic shear-velocity profiles for the eight tectonic types (Figure 10 for continents and Figure 11 for oceans) also include the average crustal parameters (V_P, V_S, density ρ and the discontinuity depths of the upper, middle, and lower crust as well of the sedimentary and water layers) extracted from the CRUST1.0 model in their reference models. The average discontinuity depth, V_P, V_S, and density of every layer for each tectonic environment are shown in Supplementary Table T2. We fix the average CRUST1.0 Moho depth for all models, apart from that for cratons, which has the crust located slightly deeper, at 40 km depth (Christensen, 1995; Mooney et al., 1998). In all the oceanic-type environments, we add a water layer with an average thickness for it and, in the case of intermediate and old oceans, a thin sedimentary layer of 70 m. A sediment layer in the continents is not necessary to explain the measurements.

For each type, we show the isotropic shear-speed profile, the V_{SH} and V_{SV} profiles, and radial anisotropy down to 700 km depth. In Supplementary Figures S3 and S4, we plot our continental and oceanic V_S models, respectively, on the background 2D histograms of the 1D shear-speed profiles extracted from the global tomographic model SL2013sv of Schaeffer and Lebedev (2013). The comparison confirms a broad consistency of the V_{SV} distributions and, also, illustrates radial anisotropy and the extent to which the isotropic average V_S profiles deviate from the V_{SV} ones due to it.

The models have substantial uncertainties for fine-scale radial variations in Vs (Section 4.3). Broader scale features, by contrast, are more robust and indicate substantial variations in shear velocities between different lithospheric types. For the global and continental models, the misfits are under 0.1% for almost all periods (Figures 8 and 10). For oceanic models (Figure 11), the misfits exceed 0.1%, in some cases, at the shortest periods included (<20 s for Rayleigh waves and <30 s for Love waves). This discrepancy is probably due to the averaging over areas with a range of different water depths and the strong, non-linear

dependence of phase velocities on the water layer thickness and crustal structure (e.g., Kustowski et al., 2007; Lebedev et al., 2013; Montagner and Jobert, 1988).

In order to illustrate better the characteristics of the shallow velocity structure and radial anisotropy, we also show the same profiles with a zoom on the crust and uppermost mantle in Supplementary Figures S5 and S6. The dispersion curves at short and intermediate periods are sensitive to the layering of shear-wave velocity within the crust. Supplementary Figures S5 and S6 illustrate the layering of the continental and oceanic crust in the different environments.

Radial anisotropy can be interpreted in terms of lattice-preferred orientation (LPO) of intrinsically anisotropic grains caused by flow due to present-day or past episodes of deformation. It thus provides crucial information on the dynamics of the lithosphere and underlying mantle (e.g., Becker and Lebedev, 2021; Fouch and Rondenay, 2006; Mainprice, 2015). Surface-wave dispersion measurements are particularly well suited to determine radial anisotropy. Our results show significant variations of radial anisotropy with depth and with the tectonic environment. In continents, positive radial anisotropy ($V_{SH} > V_{SV}$) is present within the crust and increases with depth. The best-fitting models for Phanerozoic continents and stable platforms have the strongest lower-crustal radial anisotropy, exceeding 2.5% (Supplementary Figure S5). Radial anisotropy increases in the uppermost mantle beneath continents and reaches a peak of 3-4% in the 50-100 km depth range (Figure 10). From this peak, it decreases gradually with depth down to 280-330 km, at which depth the sign of radial anisotropy flips from positive to negative beneath cratons and stable platforms. Beneath Phanerozoic continents, anisotropy is close to zero at around 260 km. Beneath rift zones, anisotropy reaches its minimum, most likely, negative, values around 200 km depth but increases to ~2% at greater depths. The depth of the anisotropy sign flip is deeper in older lithosphere types. The sign change occurs at 260 km in the Phanerozoic continents, at 300 km in stable platforms, and at 330 km in cratons.

In the oceanic models, negative anisotropy ($V_{SV} > V_{SH}$) is present in the uppermost mantle lithosphere (Figure 11 and Supplementary Figure S6). In order to confirm that the negative anisotropy in the uppermost mantle is a robust feature, we perform test inversions (Figure 12), forcing the shallow lithosphere to be isotropic down to ~50 km depth, which is where a sign change to positive is observed in real models (Figure 11). The tests show that if we fix

587 the anisotropy to zero *a priori*, the data fit worsens considerably at the short and intermediate
588 periods, even if isotropic and anisotropic structure elsewhere is allowed to vary freely,
589 indicating that negative anisotropy is required in the shallow lithospheric mantle. Below ~50
590 km depth, anisotropy is positive and increases with depth, reaching a maximum at around
591 100 km depth for all types of oceans, with the largest values exceeding 5% observed in the
592 intermediate oceans and the smallest values up to 2.6% in the backarc-average profile.
593 Below, this maximum radial anisotropy decreases and reaches negative or near-zero values at
594 220-270 km depths (Figure 11).
595
596 The overall increase in the lithospheric thickness and seismic velocities with increasing age is
597 displayed by both oceanic and continental models (Figure 13). In continents, the tectonic-
598 type-average seismic velocities and lithospheric thicknesses increase, progressively, from the
599 rift zones to Phanerozoic continents, stable platforms, and Archean cratons (Figure 13A). In
600 the oceans, the models show a strong dependence of the thickness and seismic velocity of the
601 lithosphere on its age, with velocity increasing with the age of the oceans as expected
602 (Figure 13B).
603
604 **3.4. Uncertainties of the Vs models**
605
606 We compute uncertainties of the Vs models using the model-space-projection technique
607 (Bartzsch et al., 2011; Lebedev et al., 2013). The uncertainty of each parameter, assigned to a
608 basis function sampling a certain depth range, is determined using a set of inversions. In each
609 of these inversions, the value of the parameter (the perturbation of Vs at a depth or in a depth
610 range) is fixed at a certain value, while all other parameters can vary freely. The fixed value
611 of the parameter being investigated is varied from inversion to inversion, in a broad total
612 range. The misfits yielded by these inversions form a valley, centred at the optimal model.
613 The method accounts for the trade-offs between all the inversion parameters and yields a
614 projection of the best-fitting ellipsoid in the model space onto a smaller-dimensional
615 subspace (Bartzsch et al., 2011; Lebedev et al., 2013), in this study a 1D subspace of one
616 parameter only.
617
618 Defining a threshold for the misfit, we can obtain the uncertainty for a given parameter. The
619 choice of the threshold depends on the errors in the data. An estimate of the errors in the data
620 is given by the roughness of the dispersion curve, which cannot be explained by any Earth

621 structure because of the inherent smoothness of error-free phase-velocity curves (Ravenna et
622 al. 2018; Bonadio et al. 2021). The roughness can be estimated using a weakly regularised
623 initial inversion of the phase-velocity curves for a Vs model. This model is not required to be
624 realistic and is, typically, highly oscillatory. Subtracting the dispersion curves computed for
625 this model from observed ones isolates the roughness on the latter and yields an estimate of
626 the frequency-dependent errors on the data (Ravenna et al. 2018; Bonadio et al. 2021). The
627 errors are around 0.1% at most periods, about an order of magnitude smaller than the
628 dispersion-curves errors often seen in the literature. The very small errors are thanks to the
629 averaging over large sets of points on the phase velocity maps constrained by massive,
630 accurate datasets.
631
632 We defined the misfit threshold as $M_0 + 2 (M_{min} - M_0)$, where M_0 is the root-mean-square
633 (RMS) data-synthetic misfit for the Rayleigh and Love phase velocities for the weakly
634 regularised inversion, and M_{min} is the smallest RMS misfit of all the inversions with normal
635 regularization, which combine to yield the model space projection.
636
637 We show an example on how the uncertainty is calculated at 150 km depth in the cratonic
638 profile in Figure 14. Similar calculations are performed for all the parameters in the upper
639 mantle, for all the tectonic types (Figure 15). The error bars for each parameter in Figure 15
640 are plotted at the central depth of each triangular basis function corresponding to the
641 parameter.
642
643 Importantly, the uncertainty of Vs values in the profiles depends on the width of the layer that
644 they average over and on the depth of this layer below the surface. In order to quantify this
645 dependence, we apply the model space projection to layers of different thickness, made up of
646 multiple neighbouring basis functions (Figures 16 and 17). In these experiments, parameters
647 corresponding to two or three consecutive basis functions are fixed at the same value during
648 the inversion and all other parameters can vary freely. The tests are conducted for different
649 depths in the upper mantle using the average dispersion curves of the cratons. Each of these
650 tests produces a measurement of the uncertainty for a given layer thickness and a given depth
651 (Figure 17).
652
653 The narrower the Vs depth range in question, the more uncertain the Vs value in this range is.
654 This uncertainty principle is also illustrated in Figure 18, which shows the uncertainty of the

isotropic V_S value within a depth range in the model depending on the width of the depth range (20, 50, 100 and 200 km) and its depth.

3.5. A simplified global average shear-velocity profile

Finally, we use the global average dispersion curves to compute a 1D global seismic model with minimal structural complexity in the upper mantle (Figure 19). This minimalistic 1D model is similar to the best-fitting one in terms of anisotropy but, contrary to the best-fitting models, does not show a low-velocity zone at sub-lithospheric depths, at the cost of an increase in misfit.

The V_S isotropic average is similar in appearance to the AK135 model (Kennett et al., 1995). The profile is characterized by nearly constant isotropic-average shear velocities in the upper mantle down to 200 km depth and linearly increasing shear velocities below 200 km depth. This 'AK135-style' model does not correspond to a realistic geotherm (e.g., Fullea et al., 2021; McKenzie et al., 2005). It also explains the data substantially worse than the best-fitting global seismic profile shown in Figure 8, with the synthetic-data misfit deteriorating at longer periods (misfit up to ~0.3% for Rayleigh waves and up to ~0.15% for Love waves) (Figure 14). However, such a smooth, seismic model, constrained by a large global dataset, can be used as a useful reference for seismic imaging studies.

4. Discussion

The upper mantle beneath the continents and oceans is strongly heterogeneous. Our models (Figures 10 and 11) display shear-speed values representative of the full range of different primary tectonic environments.

The best-fitting tectonic-type shear-velocity profiles can be simplified, for example by the removal of the gradients between the Moho and a ~200 km depth in the mantle (i.e., assigning a constant V_S in the depth range). Along with our global reference model, they can thus serve as useful 1D background models for seismic imaging studies at regional scales, in different tectonic environments.

The key parts of the global and tectonic-type models are the broadband phase-velocity curves

689 of the Rayleigh and Love waves. The Vs profiles that accompany them are non-unique and
690 should be viewed as representative examples of the models that fit the data. The uncertainty
691 of these models is primarily due not to random noise in the data, which is small, but to the
692 trade-offs between different model parameters, in particular seismic velocities at adjacent
693 depths. The phase-velocity component of the models gives the user the freedom to construct
694 new models, seismic or multi-parameter (e.g., Cammarano et al., 2005; Fullea et al., 2021).
695
696 Our models also include radial anisotropy profiles, prompting interesting new inferences.
697 Figure 13 shows that unlike V_S profiles, which present systematic variations with the
698 lithospheric age, radial anisotropy profiles show similar features within the oceanic and
699 continental domains. A similar observation was made based on the SEMum clustering
700 analysis by Lekic and Romanowicz (2011), who reported a peak in anisotropy at ~150 km
701 depth beneath continents and a rapid decrease below. In our profiles, anisotropy peaks at
702 around 80-100 km beneath continents and at 140-150 km depth beneath oceans and decreases
703 to around at 200-300 km depth in both cases, and changes sign to negative at greater depths
704 in most tectonic environments.
705
706 Previous studies have shown that radial anisotropy is ubiquitous in both continental and the
707 oceanic upper mantle (Beghein et al., 2006; Debayle and Kennett, 2000; Gaherty, 2004;
708 Hofmann et al., 1997; Montagner, 1994; Nishimura and Forsyth, 1989; Schlue and Knopoff,
709 1977; Visser et al., 2008). However, a consensus on the large-scale pattern of radial
710 anisotropy in the Earth's mantle has not yet been reached.
711
712 Some seismological and experimental studies report anisotropy within the MTZ (Beghein et
713 al., 2006; Guan et al., 2022; e.g., Trampert and Van Heijst, 2002; Wookey et al., 2002; Yuan
714 and Beghein, 2013), but uncertainties are large (Beghein et al., 2006) and most studies agree
715 that most of the upper mantle signal comes from above ~300 km (e.g., Kustowski et al.,
716 2007; Montagner and Kennett, 1996; Moulik and Ekström, 2014; Panning and Romanowicz,
717 2006). This has been commonly associated with the dominance of the dislocation creep
718 mechanism over diffusion creep at these depths (e.g., Gaherty and Jordan, 1995; Karato,
719 1992; Mainprice et al., 2005). Montagner and Tanimoto (1991) used a global surface-wave
720 dataset and reported anisotropy at 200–300 km depths that they interpreted as due to vertical
721 flow beneath the ridges. Gu et al. (2005) found that beneath the East Pacific Rise the faster
722 axis of radial anisotropy changed from a horizontal orientation at ~100 km depth to a vertical

orientation at ~200–300 km depth. This change in the polarity of radial anisotropy was interpreted as being due to a change in direction of mantle flow from horizontal asthenospheric shear at shallow sub-lithospheric depths to vertical flow in the deeper upper mantle beneath the ridge.

Mapping seismic anisotropy in the deep upper mantle has been challenging because the vertical resolution of most datasets decreases with depth. The data used here include a broad period range, with periods of up to ~310 s, and are sensitive to shear-wave velocity and its radial anisotropy at greater depths than in most previous studies, down to the MTZ (Fig. 2).

In Figure 20 we compare our new, global-average radial anisotropy profile with previously published ones. In the top 200 km of the mantle, positive radial anisotropy ($V_{SH} > V_{SV}$) is seen in all the models of spherically averaged anisotropy. The radial anisotropy profiles, however, show significant differences in the deep upper mantle.

The change of polarity from positive to negative values seen in our model at around 300 km depth also occurs in the Savani model (Auer et al., 2014) and BM12UM model (although only to 350 km depth) (Burgos et al., 2014). SEMUCB-WM1 (French and Romanowicz, 2014) and SGLOBE-rani (Chang et al., 2015) models show a slightly negative anisotropy (less than 1%) as well but at greater depths, within the MTZ. SAW642AN (Panning and Romanowicz, 2006) and the model of Visser et al. (2008) indicate a slightly shallower (200-250 km depth) flip to negative values (Figure 20). Our new model shows negative anisotropy ($V_{SV} > V_{SH}$) down to the bottom of the MTZ. As illustrated in Figure 2, the resolution of the anisotropy decreases below 400 km depth, but there is still substantial data sensitivity to it, even though we may not be resolving the depth variations as well as at shallower depths.

The model-space-projection method yields an estimate of 0.61% for the uncertainty of anisotropy across the 300-660 depth range (Figure 21). At a single point, the uncertainty would be much larger—in our model and in any other model. But over the broader depth range, anisotropy is constrained much tighter, as is Vs (Figures 16-18). The tests thus confirm that anisotropy is most likely to be negative in the lower half of the upper mantle. Another series of tests shows that the uncertainty of anisotropy in the top 50 km of the lithosphere beneath “intermediate” oceans is 2.51%, validating the observation of negative anisotropy there (Figure 21).

Model disagreements indicate that the effects of radial anisotropy on seismic data still cannot be easily separated from the effects of the isotropic structure. The discrepancies between radially anisotropic models may result from data uncertainties, poor data coverage, or the use of different modeling techniques (e.g., Chang et al., 2014). The influence of the crust on surface waves can also be responsible for some differences in the mantle (Levshin and Ratnikova, 1984), even though a priori crustal models are usually included in the inversion to account for this effect (e.g., Bozdağ et al., 2011; Ferreira et al., 2010; Kustowski et al., 2008).

Radial anisotropy is universally accepted to be present in the upper ~200 km of the mantle (e.g., Dziewonski and Anderson, 1981). Intriguing lateral variations have been observed, particularly in the oceanic basins (Gung et al., 2003; Hofmann et al., 1997). Efforts to map seismic anisotropy in the oceans range in scale from global surface-wave studies to regional experiments (e.g., Beghein et al., 2014; French and Romanowicz, 2014; Hofmann et al., 1997; Montagner, 2002; Moulik and Ekström, 2014; Russell et al., 2022, 2019; Takeo et al., 2018, 2013). Nonetheless, an agreement between them, especially at shallow mantle lithospheric depths, is relatively poor. Below the oceanic lithosphere, V_{SH} generally exceeds V_{SV} by a few percent (Kustowski et al., 2008; Nishimura and Forsyth, 1989; Shapiro and Ritzwoller, 2002), a pattern expected for horizontal flow. Regan and Anderson (1984) were the first to present radial anisotropy models of the upper mantle based on a tectonic regionalization of the oceans and reported $V_{SH} > V_{SV}$ nearly everywhere, apart from the East Pacific Rise, where they found $V_{SV} > V_{SH}$ at 100-220 depth, consistent with ascending flow. Along the southern East Pacific Rise, azimuthal anisotropy of short-period Rayleigh waves reaches a minimum at the ridge axis (Forsyth et al., 1998), consistent with either a component of vertical upwelling or not yet established horizontal flow. The radially anisotropic model of the Pacific upper mantle by Hofmann et al. (1997) displays a broad anomaly in radial anisotropy in the northern Pacific, with its centre near Hawaii. The 5% amplitude of this anomaly, which reaches a maximum at 150 km depth, has been confirmed by Boschi and Ekström (2002). At regional scales, some recent studies using ocean-bottom seismometers and higher frequency surface waves, sensitive to the shallow lithosphere, reported $V_{SH} > V_{SV}$ in shallow oceanic lithosphere (e.g., Russell et al., 2019; Takeo et al., 2013; Yang et al., 2020). This adds to the evidence from the active-source experiments in the Pacific that indicated strong azimuthal anisotropy in the uppermost mantle (e.g., Kodaira et al., 2014; Mark et al., 2019; Morris et al., 1969; VanderBeek and Toomey, 2017).

Our results provide new evidence on shear-wave anisotropy at lithospheric and asthenospheric depths, based on a very broadband surface-wave dataset. We observe $V_{SH} < V_{SV}$ in the shallow oceanic lithosphere. Some indications for this feature can be seen in some of the previous models (Burgos et al., 2014; Moulik and Ekström, 2014), although many other models do not contain it—possibly, in part, due to the relatively course parametrization often used for the uppermost mantle in large-scale studies.

The negative anisotropy can be explained by radial flow beneath spreading centres. If so, this fabric is likely to be frozen into the lithosphere close to the ridges. The deeper part of the lithosphere is formed later, as the plate thickens while moving above and shearing the underlying asthenosphere, and this is where we observe $V_{SH} > V_{SV}$.

The shallow mantle lithosphere beneath the oceans thus shows both negative radial anisotropy ($V_{SH} < V_{SV}$), consistent with vertical flow at the time of its formation, and azimuthal anisotropy with fast-propagation directions aligned with the paleo-spreading (e.g., Becker et al., 2014; Schaeffer et al., 2016), which is consistent with spreading-parallel horizontal flow. In the vicinity of the ridge, where the upper lithosphere forms, vertical flow upwards coexists with the horizontal flow away from the ridge. Our observations show that the preferential alignment of the olivine crystals within the lithosphere reflects this corner flow. A significant proportion of the olivine crystals are likely to be oriented vertically, and a significant proportion of the remaining ones along the spreading-parallel horizontal flow lines. V_S anisotropy in olivine, the dominant mineral in the upper mantle, is around 18% (e.g., Mainprice et al., 2000). Thus, negative radial anisotropy of a few percent and azimuthal anisotropy of a few percent can be accounted for by the preferential alignment of some of the olivine crystals in the vertical direction and some of the crystals—in the spreading-parallel horizontal direction.

5. Concluding remarks

The recent increase in the global sampling of the Earth with seismic data presents an opportunity to produce new models of the upper mantle at global and regional scales, constrained by very large surface-wave datasets. Our new set of pairs of Rayleigh and Love phase-velocity curves for the Earth's main tectonic environments spans a very broad period

range and presents useful data for the creation of seismic or multi-parameter 1D models. Example 1D seismic models fit the data very closely, with misfits under 0.1% at most periods. The Vs uncertainty in these models is large for Vs variations in small depth ranges (thin layers) but decreases with an increasing layer thickness.

Seismic velocities and the inferred lithospheric thickness vary systematically with the age of the lithosphere in both continents and oceans. A change in the sign of radial anisotropy from positive to negative values at ~200-300 km depth is observed and well constrained in both the global and most tectonic-type models. In the young, intermediate, and old age oceanic models, substantial negative anisotropy in the shallow mantle lithosphere, down to ~50 km depth, is required by the data. A minimum-complexity, global-average 1D profile can be used as a smooth initial model in tomography and other imaging analyses.

Surface waves are highly sensitive to the Vs and thermal structure of the lithosphere and underlying upper mantle. Yet, the uncertainty of Vs models yielded by the inversion of surface wave data—even when they are very accurate and span a broad period range—is large at the radial length scales comparable to the entire thickness of the mantle lithosphere in thin-lithosphere environments. Accurate additional information is required in order to reduce the uncertainty of the profiles and can be incorporated into multi-parameter thermodynamic inversions of surface-wave data (e.g., Cammarano et al., 2005; Fullea et al., 2021; Lebedev et al. 2023).

Acknowledgements

We thank the Editor, Martin Mai, and two anonymous reviewers for valuable suggestions. We thank Andrew Schaeffer for providing his regionalisation map and his 1D V_S profiles, and Nicolas L. Celli for assistance in the phase velocity map calculations. We are grateful to the operators of seismic networks and arrays who have created and made available the broadband seismic data that was used in the original measurements. We thank the all the data centers for providing the waveform data used. This work was supported by the Science Foundation Ireland (SFI) grants 13/CDA/2192 and 16/IA/4598, the latter co-funded by the Geological Survey of Ireland and the Marine Institute, and the UK Natural Environment Research Council grant XE/X000060/1. The research has been completed in the framework of the projects 3D Earth and 4D Earth, funded by the European Space Agency (ESA) as a Support to Science Element (STSE). C.C. acknowledges the grant CEX2019-000928-S funded by AEI 10.13039/501100011033. Plotting of the figures has been done with Generic Mapping Tools (GMT) (Wessel et al., 2013).

Data and Resources

The waveform data are freely available from several data centers including the Incorporated Research Institutions for Seismology Data Management Center (IRIS-DMC, https://ds.iris.edu/ds/nodes/dmc); the GEOFON Data Centre of the GFZ (https://geofon.gfz-potsdam.de/waveform/archive); the RESIF seismic data portal (https://seismology.resif.fr); ORFEUS (http://orfeus-eu.org/webdc3); the National Observatory of Athens NOA (http://bbnet.gein.noa.gr); the Turkish Earthquake Research Institute KOERI (http://eida-service.koeri.boun.edu.tr); and the Italian Istituto Nazionale di Geofisica e Vulcanologia INGV (http://webservices.ingv.it). The global and tectonic-type dispersion curves and 1D seismic-velocity models will be deposited and made publicly available. The Supplementary Material includes two tables and six figures. The tables indicate the parameters used for each layer of the crust in the background models. Figures S1, S3, and S4 show the 1D models together with the density of the 1D profiles extracted from the global tomographic model SL2013sv. Figures S2, S5, and S6 illustrate the global and tectonic-type models with a zoom on the top 50 km.

Declaration of Competing Interests

881

882 The authors declare no competing interests.

883

884 **References**

885

886 Agius, M.R., Lebedev, S., 2014. Shear-velocity structure, radial anisotropy and dynamics of
887 the tibetan crust. Geophysical Journal International 199, 1395–1415.
888 https://doi.org/10.1093/gji/ggu326
889 Agius, M.R., Lebedev, S., 2013. Tibetan and Indian lithospheres in the upper mantle beneath
890 Tibet : Evidence from broadband surface-wave dispersion 14, 4260–4281.
891 https://doi.org/10.1002/ggge.20274
892 Anderson, D.L., 1999. A theory of the Earth: Hutton and Humpty Dumpty and Holmes.
893 Geological Society Special Publication 150, 13–35.
894 https://doi.org/10.1144/GSL.SP.1999.150.01.02
895 Anderson, D.L., 1979. The Deep Structure of Continents. Journal of Geophysical Research
896 84, 3–8.
897 Anderson, D.L., 1961. Elastic Wave Propagation in Layered Anisotropic Media. Journal of
898 Geophysical Research 66, 54–62.
899 Auer, L., Boschi, L., Becker, T.W., Nissen-Meyer, T., Giardini, D., 2014. Savani: A variable
900 resolution whole-mantle model of anisotropic shear velocity variations based on
901 multiple data sets. Journal of Geophysical Research: Solid Earth 119, 3006–3034.
902 https://doi.org/10.1002/2013JB010773
903 Bartzsch, S., Lebedev, S., Meier, T., 2011. Resolving the lithosphere-asthenosphere boundary
904 with seismic Rayleigh waves. Geophysical Journal International 186, 1152–1164.
905 https://doi.org/10.1111/j.1365-246X.2011.05096.x
906 Bastow, I.D., Nyblade, A.A., Stuart, G.W., Rooney, T.O., Benoit, M.H., 2008. Upper mantle
907 seismic structure beneath the Ethiopian hot spot: Rifting at the edge of the African
908 low-velocity anomaly. Geochemistry, Geophysics, Geosystems 9, Q12022.
909 Becker, T.W., Conrad, C.P., Schaeffer, A.J., Lebedev, S., 2014. Origin of azimuthal seismic
910 anisotropy in oceanic plates and mantle. Earth and Planetary Science Letters 401,
911 236–250. https://doi.org/10.1016/j.epsl.2014.06.014
912 Becker, T.W., Lebedev, S., 2021. Dynamics of the Upper Mantle in Light of Seismic
913 Anisotropy, in: Mantle Convection and Surface Expressions, Geophysical
914 Monograph,. Marquardt H., Ballmer M., Cottaar S., Jasper K., American Geophysical
915 Union (AGU), pp. 259–282. https://doi.org/10.1002/9781119528609.ch10
916 Beghein, C., Trampert, J., van Heijst, H.J., 2006. Radial anisotropy in seismic reference
917 models of the mantle. Journal of Geophysical Research: Solid Earth 111, 1–9.
918 https://doi.org/10.1029/2005JB003728
919 Beghein, C., Yuan, K., Schmerr, N., Xing, Z., 2014. Changes in seismic anisotropy shed light
920 on the nature of the Gutenberg discontinuity. Science 343, 1237–1240.
921 https://doi.org/10.1126/science.1246724
922 Beucler, É., Montagner, J.-P., 2006. Computation of Large Anisotropic Seismic
923 Heterogeneities (CLASH). Geophysical Journal International 165, 447–468.
924 https://doi.org/10.1111/j.1365-246X.2005.02813.x
925 Bonadio, R., Lebedev, S., Meier, T., Arroucau, P., Schaeffer, A.J., Licciardi, A., Agius,
926 M.R., Horan, C., Collins, L., O'Reilly, B.M., Readman, P.W., 2021. Optimal
927 resolution tomography with error tracking and the structure of the crust and upper
928 mantle beneath Ireland and Britain. Geophysical Journal International 226, 2158–
929 2188. https://doi.org/10.1093/gji/ggab169
930 Boschi, L., Ekström, G., 2002. New images of the Earth's upper mantle from measurements
931 of surface wave phase velocity anomalies. Journal of Geophysical Research: Solid
932 Earth 107, ESE 1-1-ESE 1-14. https://doi.org/10.1029/2000jb000059

Boyce, A., Bastow, I.D., Cottaar, S., Kounoudis, R., De Courbeville, J.G., Caunt, E., Desai, S., 2021. AFRP20: New P-wavespeed Model for the African Mantle Reveals Two Whole-Mantle Plumes Below East Africa and Neoproterozoic Modification of the Tanzania Craton. Geochemistry, Geophysics, Geosystems 22, e2020GC009302.

Bozdağ, E., Peter, D., Lefebvre, M., Komatitsch, D., Tromp, J., Hill, J., Podhorszki, N., Pugmire, D., 2016. Global adjoint tomography: First-generation model. Geophysical Journal International 207, 1739–1766. https://doi.org/10.1093/gji/ggw356

Bozdağ, E., Trampert, J., Tromp, J., 2011. Misfit functions for full waveform inversion based on instantaneous phase and envelope measurements: Misfit functions for full waveform inversion. Geophysical Journal International 185, 845–870. https://doi.org/10.1111/j.1365-246X.2011.04970.x

Brune, J., Dorman, J., 1963. Seismic waves and Earth structure in the Canadian shield 53, 167–210.

Burgos, G., Montagner, J., Beucler, E., Capdeville, Y., Mocquet, A., Drilleau, M., 2014. Oceanic lithosphere-asthenosphere boundary from surface wave dispersion data. Journal of Geophysical Research : Solid Earth 119, 1079–1093. https://doi.org/10.1002/2013JB010528.Abstract

Cammarano, F., Deuss, A., Goes, S., Giardini, D., 2005. One-dimensional physical reference models for the upper mantle and transition zone: Combining seismic and mineral physics constraints. Journal of Geophysical Research: Solid Earth 110. https://doi.org/10.1029/2004JB003272

Celli, N.L., Lebedev, S., Schaeffer, A., Gaina, C., 2020. African cratonic lithosphere carved by mantle plumes. Nature Communications 11, 92. https://doi.org/10.1038/s41467-019-13871-2

Celli, N.L., Lebedev, S., Schaeffer, A.J., Gaina, C., 2021. The tilted Iceland Plume and its effect on the North Atlantic evolution and magmatism. Earth and Planetary Science Letters 569, 117048. https://doi.org/10.1016/j.epsl.2021.117048

Chagas De Melo, B., Lebedev, S., Celli, N., Assumpção, M., 2022. Detailed Structure of the South American Cratons Using Waveform Tomography.

Chang, S.J., Ferreira, A.M.G., Ritsema, J., Heijst, H.J., Woodhouse, J.H., 2015. Joint inversion for global isotropic and radially anisotropic mantle structure including crustal thickness perturbations. Journal of Geophysical Research : Solid Earth 120, 4278–4300. https://doi.org/10.1002/2014JB011824.Received

Chang, S.-J., Ferreira, A.M.G., Ritsema, J., Van Heijst, H.J., Woodhouse, J.H., 2014. Global radially anisotropic mantle structure from multiple datasets: A review, current challenges, and outlook. Tectonophysics 617, 1–19. https://doi.org/10.1016/j.tecto.2014.01.033

Christensen, N.I., 1995. Seismic velocity structure and composition of the continental crust : A global view 100, 9761–9788.

Civiero, C., Armitage, J.J., Goes, S., Hammond, J.O.S., 2019. The Seismic Signature of Upper-Mantle Plumes: Application to the Northern East African Rift. Geochemistry, Geophysics, Geosystems 20, 6106–6122. https://doi.org/10.1029/2019GC008636

Civiero, C., Hammond, J.O.S., Goes, S., Fishwick, S., Ahmed, A., Ayele, A., Doubre, C., Goitom, B., Keir, D., Kendall, J.M., Leroy, S., Ogubazghi, G., Rümpker, G., Stuart, G.W., 2015. Multiple mantle upwellings in the transition zone beneath the northern East-African Rift system from relative P-wave travel-time tomography. Geochemistry, Geophysics, Geosystems 16, 2949–2968. https://doi.org/10.1002/2015GC005948

Civiero, C., Lebedev, S., Celli, N.L., 2022. A Complex Mantle Plume Head Below East Africa-Arabia Shaped by the Lithosphere-Asthenosphere Boundary Topography Geochemistry , Geophysics , Geosystems. https://doi.org/10.1029/2022GC010610

Dalton, C.A., Ekström, G., 2006. Global models of surface wave attenuation. Journal of Geophysical Research: Solid Earth 111, 1–19. https://doi.org/10.1029/2005JB003997

Dalton, C.A., Ekström, G., Dziewonski, A.M., 2009. Global seismological shear velocity and attenuation: A comparison with experimental observations. Earth and Planetary Science Letters 284, 65–75. https://doi.org/10.1016/j.epsl.2009.04.009

Dannberg, J., Eilon, Z., Faul, U., Gassmöller, R., Moulik, P., Myhill, R., 2017. The importance of grain size to mantle dynamics and seismological observations. Geochem Geophys Geosyst 18, 3034–3061. https://doi.org/10.1002/2017GC006944

De Laat, J.I., Lebedev, S., Celli, N.L., Bonadio, R., de Melo, B.C., Rawlinson, N., 2023. Structure and evolution of the Australian Plate and underlying upper mantle from waveform tomography with massive datasets. Geophysical Journal International ggad062. https://doi.org/10.1093/gji/ggad062

Debayle, E., Kennett, B.L.N., 2000. The Australian continental upper mantle: Structure and deformation inferred from surface waves. Journal of Geophysical Research 105, 25,423-25,450.

Debayle, E., Ricard, Y., 2012. A global shear velocity model of the upper mantle from fundamental and higher Rayleigh mode measurements: GLOBAL SHEAR WAVE VELOCITY DISTRIBUTION. J. Geophys. Res. 117. https://doi.org/10.1029/2012JB009288

Durand, S., Debayle, E., Ricard, Y., 2015. Rayleigh wave phase velocity and error maps up to the fifth overtone. Geophysical Research Letters 42, 3266–3272. https://doi.org/10.1002/2015GL063700

Dziewonski, A.M., Anderson, D.L., 1981. Preliminary reference Earth model. Physics of the Earth and Planetary Interiors 25, 297–356. https://doi.org/10.1016/0031-9201(81)90046-7

Dziewonski, A.M., Chou, T.A., Woodhouse, J.H., 1981. Determination of earthquake source parameters from waveform data for studies of global and regional seismicity. Journal of Geophysical Research 86, 2825–2852. https://doi.org/10.1029/JB086iB04p02825

Ekström, G., 2011. A global model of Love and Rayleigh surface wave dispersion and anisotropy, 25-250s. Geophysical Journal International 187, 1668–1686. https://doi.org/10.1111/j.1365-246X.2011.05225.x

Ekström, G., Nettles, M., Dziewoński, A.M., 2012. The global CMT project 2004-2010: Centroid-moment tensors for 13,017 earthquakes. Physics of the Earth and Planetary Interiors 200–201, 1–9. https://doi.org/10.1016/j.pepi.2012.04.002

Ekström, G., Tromp, J., Larson, E.W.F., 1997. Measurements and global models of surface wave propagation. Journal of Geophysical Research: Solid Earth 102, 8137–8157.

Endrun, B., Meier, T., Lebedev, S., Bohnhoff, M., Stavrakakis, G., Harjes, H.P., 2008. S velocity structure and radial anisotropy in the Aegean region from surface wave dispersion. Geophysical Journal International 174, 593–616. https://doi.org/10.1111/j.1365-246X.2008.03802.x

Faul, U.H., Jackson, I., 2005. The seismological signature of temperature and grain size variations in the upper mantle. Earth and Planetary Science Letters 234, 119–134. https://doi.org/10.1029/2001JB001225

Ferreira, A.M.G., Woodhouse, J.H., Visser, K., Trampert, J., 2010. On the robustness of global radially anisotropic surface wave tomography. J. Geophys. Res. 115, B04313. https://doi.org/10.1029/2009JB006716

Forsyth, D.W., Webb, S.C., Dorman, L.M., Shen, Y., 1998. Phase velocities of Rayleigh waves across the East Pacific Rise. Science 280, 5367. https://doi.org/10.1016/0040-1951(70)90113-7

Foster, A., Nettles, M., Ekström, G., 2014. Overtone Interference in array-based love-wave phase measurements. Bulletin of the Seismological Society of America 104, 2266–2277. https://doi.org/10.1785/0120140100

Fouch, M.J., Rondenay, S., 2006. Seismic anisotropy beneath stable continental interiors. Physics of the Earth and Planetary Interiors 158, 292–320. https://doi.org/10.1016/j.pepi.2006.03.024

French, S., Lekic, V., Romanowicz, B., 2013. Waveform tomography reveals channeled flow at the base of the oceanic asthenosphere. Science 342, 227–230. https://doi.org/10.1126/science.1241514

French, S.W., Romanowicz, B.A., 2014. Whole-mantle radially anisotropic shear velocity structure from spectral-element waveform tomography. Geophysical Journal International 199, 1303–1327. https://doi.org/10.1093/gji/ggu334

Fullea, J., Lebedev, S., Agius, M.R., Jones, A.G., Afonso, J.C., 2012. Lithospheric structure in the Baikal-central Mongolia region from integrated geophysical-petrological inversion of surface-wave data and topographic elevation. Geochemistry, Geophysics, Geosystems 13, 1–20. https://doi.org/10.1029/2012GC004138

Fullea, J., Lebedev, S., Martinec, Z., Celli, N.L., 2021. WINTERC-grav: mapping the upper mantle thermochemical heterogeneity from coupled geophysical-petrological inversion of seismic waveforms, heat flow, surface elevation and gravity satellite data. Geophysical Journal International 226, 146–191.

Gaherty, J.B., 2004. A surface wave analysis of seismic anisotropy beneath eastern North America. Geophysical Journal International 158, 1053–1066. https://doi.org/10.1111/j.1365-246X.2004.02371.x

Gaherty, J.B., Jordan, T.H., 1995. Lehmann Discontinuity as the Base of an Anisotropic Layer Beneath Continents. Advancement Of Science 268, 1468–1471.

Grand, S.P., Helmberger, D.V., 1984. Upper mantle shear structure of North America. Journal of Geophysical Research 76, 399–438. https://doi.org/10.1029/JB079i026p04017

Gu, Y.J., Lerner-Lam, A.L., Dziewonski, A.M., Ekström, G., 2005. Deep structure and seismic anisotropy beneath the East Pacific Rise. Earth and Planetary Science Letters 232, 259–272. https://doi.org/10.1016/j.epsl.2005.01.019

Guan, L., Yamazaki, D., Tsujino, N., Tange, Y., Higo, Y., 2022. Seismic Anisotropy in the Lower Mantle Transition Zone Induced by Lattice Preferred Orientation of Akimotoite. Geophysical Research Letters 49. https://doi.org/10.1029/2022GL098549

Gung, Y., Panning, M., Romanowicz, B., 2003. Global anisotropy and the thickness of continents. Nature 422, 707–711. https://doi.org/10.1038/nature01559

Gutenberg, B., 1953. Wave velocities at depths between 50 and 660 kilometers. Bulletin - Seismological Society of America 43, 223–232.

Hales, A.L., 1991. Upper mantle models and the thickness of the continental lithosphere. Geophysical Journal International 105, 355–363. https://doi.org/10.1111/j.1365-246X.1991.tb06718.x

Hariharan, A., Dalton, C.A., Ma, Z., Ekström, G., 2020. Evidence of Overtone Interference in Fundamental-Mode Rayleigh Wave Phase and Amplitude Measurements. Journal of Geophysical Research: Solid Earth 125, 1–17. https://doi.org/10.1029/2019JB018540

Herrin, E., 1968. Seismological tables for P phases. Bulletin of the Seismological Society of America 58, 288–288. https://doi.org/10.1086/622062

Hofmann, C., Courtillot, V., Féraud, G., Rochette, P., Yirgu, G., Pik, R., 1997. Timing of the Ethiopian floodbasalt event and implications forplume birthand global change. Nature 246, 170. https://doi.org/10.1038/246170a0

Jeffreys, H., Bullen, K.E., 1958. Seismological Tables. Br. Assoc. Adv. Sci.

Karato, S., 1992. On the Lehmann discontinuity. Geophysical Research Letters 19, 2255–2258.

Kennett, B.L.N., Engdahl, E.R., 1991. Traveltimes for global earthquake location and phase identification. Geophys. J. Int. 105, 429–465. https://doi.org/DOI 10.1111/j.1365-246X.1991.tb06724.x

Kennett, B.L.N., Engdahl, E.R., Buland, R., 1995. Constraints on seismic velocities in the Earth from travel times. Geophysical Journal International 122, 108–124. https://doi.org/10.1111/j.1365-246X.1995.tb03540.x

Kennett, B.L.N., van der Hilst, R.D., 1998. Seismic Structure of the Mantle: From Subduction Zone to Craton, in: The Earth's Mantle: Composition, Structure, and Evolution. pp. 381–404.

Kodaira, S., Fujie, G., Yamashita, M., Sato, T., Takahashi, T., 2014. Seismological evidence of mantle flow driving plate motions at a palaeo-spreading centre. Nature Geoscience 7, 371–375. https://doi.org/10.1038/NGEO2121

Kustowski, B., Dziewonski, A.M., Ekstrom, G., 2007. Nonlinear Crustal Corrections for Normal-Mode Seismograms. Bulletin of the Seismological Society of America 97, 1756–1762. https://doi.org/10.1785/0120070041

Kustowski, B., Ekström, G., Dziewoński, A.M., 2008. Anisotropic shear-wave velocity structure of the earth's mantle: A global model. Journal of Geophysical Research: Solid Earth 113, 1–23. https://doi.org/10.1029/2007JB005169

Laske, G., 1995. Global observation of off-great-circle propagation of long-period surface waves. Geophysical Journal International 245–259.

Laske, G., Masters, G., Ma, Z., Pasyanos, M.E., 2013. CRUST1.0: An Updated Global Model of Earth's Crust. Geophys. Res. Abstracts 15, Abstract EGU2013--2658.

Lavoué, F., Lebedev, S., Celli, N., Schaeffer, A., 2021. Radially and azimuthally anisotropic shear-wave velocity model of the Earth's upper mantle, in: EGU General Assembly Conference Abstracts, EGU General Assembly Conference Abstracts. pp. EGU21-14987. https://doi.org/10.5194/egusphere-egu21-14987

Lebedev, S., Adam, J.M.C., Meier, T., 2013. Mapping the Moho with seismic surface waves: A review, resolution analysis, and recommended inversion strategies. Tectonophysics 609, 377–394. https://doi.org/10.1016/j.tecto.2012.12.030

Lebedev, S., Meier, T., Hilst, R.D.V.D., 2006. Asthenospheric flow and origin of volcanism in the Baikal Rift area. Earth and Planetary Science Letters 249, 415–424. https://doi.org/10.1016/j.epsl.2006.07.007

Lebedev, S., Nolet, G., Meier, T., van der Hilst, R.D., 2005. Automated multimode inversion of surface and S waveforms. Geophysical Journal International 162, 951–964. https://doi.org/10.1111/j.1365-246X.2005.02708.x

Lebedev, S., Van Der Hilst, R.D., 2008. Global upper-mantle tomography with the automated multimode inversion of surface and S-wave forms. Geophysical Journal International 173, 505–518. https://doi.org/10.1111/j.1365-246X.2008.03721.x

Legendre, C.P., Meier, T., Lebedev, S., Friederich, W., Viereck-Götte, L., 2012. A shear wave velocity model of the European upper mantle from automated inversion of seismic shear and surface waveforms. Geophysical Journal International 191, 282–304. https://doi.org/10.1111/j.1365-246X.2012.05613.x

1127 Lehmann, I., 1961. S and the Structure of the Upper Mantle. Geophysical Journal of the
1128 Royal Astronomical Society 4, 124–138. https://doi.org/10.1111/j.1365-
1129 246X.1961.tb06808.x
1130 Lekic, V., Romanowicz, B., 2011. Tectonic regionalization without a priori information: A
1131 cluster analysis of upper mantle tomography. Earth and Planetary Science Letters 308,
1132 151–160. https://doi.org/10.1016/j.epsl.2011.05.050
1133 Levshin, A., Ratnikova, L., 1984. Apparent ansiotropy in inhomogeneous media.
1134 Geophysical Journal International 76, 65–69. https://doi.org/10.1111/j.1365-
1135 246X.1984.tb05022.x
1136 Ma, Z., Masters, G., Laske, G., Pasyanos, M., 2014. A comprehensive dispersion model of
1137 surface wave phase and group velocity for the globe. Geophysical Journal
1138 International 199, 113–135. https://doi.org/10.1093/gji/ggu246
1139 Mainprice, D., 2015. Seismic Anisotropy of the Deep Earth from a Mineral and Rock Physics
1140 Perspective. Treatise on Geophysics: Second Edition 2, 487–538.
1141 https://doi.org/10.1016/B978-0-444-53802-4.00044-0
1142 Mainprice, D., Barruol, G., Ismaïl, W.B., 2000. The seismic anisotropy of the Earth's mantle:
1143 from single crystal to polycrystal. American Geophysical Union.
1144 Mainprice, D., Tommasi, A., Couvy, H., Cordier, P., Frost, D.J., 2005. Pressure sensitivity of
1145 olivine slip systems and seismic anisotropy of Earth's upper mantle. Nature 433, 731–
1146 733. https://doi.org/10.1038/nature03266
1147 Mark, H.F., Lizarralde, D., Collins, J.A., 2019. Azimuthal Seismic Anisotropy of 70-Ma
1148 Pacific-Plate Upper Mantle. Journal of Geophysical Research : Solid Earth 124,
1149 1889–1909. https://doi.org/10.1029/2018JB016451
1150 Masters, G., Jordan, T.H., Silver, P.G., Gilbert, F., 1982. Aspherical Earth structure from
1151 fundamental spheroidal-mode data. Nature 298, 609–613.
1152 https://doi.org/10.1038/298609a0
1153 McEvilly, T.V., 1964. Central U.S. crust- Upper mantle structure from Love and Rayleigh
1154 wave phase velocity inversion. Bulletin of the Seismological Society of America 54,
1155 1997–2015.
1156 McKenzie, D., Jackson, J., Priestley, K., 2005. Thermal structure of oceanic and continental
1157 lithosphere. Earth and Planetary Science Letters 233, 337–349.
1158 https://doi.org/10.1016/j.epsl.2005.02.005
1159 Meier, T., Dietrich, K., Stöckhert, B., Harjes, H.P., 2004. One-dimensional models of shear
1160 wave velocity for the eastern Mediterranean obtained from the inversion of Rayleigh
1161 wave phase velocities and tectonic implications. Geophysical Journal International
1162 156, 45–58. https://doi.org/10.1111/j.1365-246X.2004.02121.x
1163 Montagner, J.P., 2007. Deep Earth Structure - Upper Mantle Structure: Global Isotropic and
1164 Anisotropic Elastic Tomography. Treatise on Geophysics: Second Edition 1, 613–
1165 639. https://doi.org/10.1016/B978-0-444-53802-4.00016-6
1166 Montagner, J.P., 2002. Upper mantle low anisotropy channels below the Pacific Plate. Earth
1167 and Planetary Science Letters 202, 263–274. https://doi.org/10.1016/S0012-
1168 821X(02)00791-4
1169 Montagner, J.-P., 1994. Can seismology tell us anything about convection in the mantle?
1170 Reviews of Geophysics 32, 115–137. https://doi.org/10.1029/94RG00099
1171 Montagner, J.-P., Jobert, N., 1988. Vectorial tomography - 11. Application to the Indian
1172 Ocean. Geophysical Journal 94, 309–344.
1173 Montagner, J.P., Kennett, B.L.N., 1996. How to reconcile body-wave and normal-mode
1174 reference earth models. Geophysical Journal International 125, 229–248.
1175 https://doi.org/10.1111/j.1365-246X.1996.tb06548.x

Montagner, J.P., Tanimoto, T., 1991. Global upper mantle tomography of seismic velocities and anisotropies. Journal of Geophysical Research 96. https://doi.org/10.1029/91jb01890
Mooney, W.D., Laske, G., Masters, T.G., 1998. CRUST 5.1: A global crustal model at 5° × 5°. Journal of Geophysical Research: Solid Earth 103, 727–747. https://doi.org/10.1029/97jb02122
Morelli, A., Dziewonski, A.M., 1993. Body Wave Traveltimes and A Spherically Symmetric P- and S-Wave Velocity Model. Geophysical Journal International 112, 178–194. https://doi.org/10.1111/j.1365-246X.1993.tb01448.x
Morris, G.B., Raitt, R.W., Shor, G., 1969. Velocity Anisotropy and Delay-Time Maps of the Mantle Near Hawaii. J Geophys Res 74, 4300–4316. https://doi.org/10.1029/jb074i017p04300
Moulik, P., Ekström, G., 2014. An anisotropic shear velocity model of the Earth's mantle using normal modes, body waves, surface waves and long-period waveforms. Geophysical Journal International 199, 1713–1738. https://doi.org/10.1093/gji/ggu356
Moulik, P., Lekic, V., Romanowicz, B., Ma, Z., Schaeffer, A., Ho, T., Beucler, E., Debayle, E., Deuss, A., Durand, S., Ekstr, G., 2021. Global Reference Seismological Datasets : Multi-mode Surface Wave Dispersion. Geophysical Journal International 228, 1808–1849.
Nettles, M., Dziewoński, A.M., 2011. Effect of higher-mode interference on measurements and models of fundamental-mode surface-wave dispersion. Bulletin of the Seismological Society of America 101, 2270–2280. https://doi.org/10.1785/0120110019
Nishimura, C.E., Forsyth, D.W., 1989. The anisotropic structure of the upper mantle in the Pacific. Geophysical Journal International 96, 203–229. https://doi.org/10.1111/j.1365-246X.1989.tb04446.x
Nishimura, C.E., Forsyth, D.W., 1988. Rayleigh wave phase velocities in the Pacific with implications for azimuthal anisotropy and lateral heterogeneities. Geophysical Journal 94, 479–501. https://doi.org/10.1111/j.1365-246X.1988.tb02270.x
Nolet, G., 2008. A Breviary of Seismic Tomography: Imaging the Interior of the Earth and Sun, A Breviary of Seismic Tomography. Cambridge University Press.
Nolet, G., Grand, S.P., Kennett, B.L.N., 1994. Seismic heterogeneity in the upper mantle. Journal of Geophysical Research 99, 753–766. https://doi.org/10.1029/94jb01892
Panning, M., Romanowicz, B., 2006. A three-dimensional radially anisotropic model of shear velocity in the whole mantle. Geophysical Journal International 167, 361–379. https://doi.org/10.1111/j.1365-246X.2006.03100.x
Ravenna, M., Lebedev, S., 2018. Bayesian inversion of surface-wave data for radial and azimuthal shear-wave anisotropy, with applications to central Mongolia and west-central Italy. Geophysical Journal International 213, 278–300. https://doi.org/10.1093/gji/ggx497
Regan, J., Anderson, D.L., 1984. Anisotropic Models of the Upper Mantle. Physics of the Earth and Planetary Interiors 37–72.
Revenaugh, J., Jordan, T.H., 1991. Mantle layering from ScS reverberations 3. The upper mantle. Journal of Geophysical Research 96. https://doi.org/10.1029/91jb01487
Ritsema, J., Deuss, A., Van Heijst, H.J., Woodhouse, J.H., 2011. S40RTS: A degree-40 shear-velocity model for the mantle from new Rayleigh wave dispersion, teleseismic traveltime and normal-mode splitting function measurements. Geophysical Journal International 184, 1223–1236. https://doi.org/10.1111/j.1365-246X.2010.04884.x
Russell, J.B., Gaherty, J.B., Lin, P.Y.P., Lizarralde, D., Collins, J.A., Hirth, G., Evans, R.L., 2019. High-Resolution Constraints on Pacific Upper Mantle Petrofabric Inferred

From Surface-Wave Anisotropy. Journal of Geophysical Research: Solid Earth 124, 631–657. https://doi.org/10.1029/2018JB016598
Russell, J.B., Gaherty, J.B., Mark, H.F., Hirth, G., Hansen, L.N., Lizarralde, D., Collins, J.A., Evans, R.L., 2022. Seismological Evidence for Girdled Olivine Lattice-Preferred Orientation in Oceanic Lithosphere and Implications for Mantle Deformation Processes During Seafloor Spreading. Geochemistry, Geophysics, Geosystems 23, 1–22. https://doi.org/10.1029/2022GC010542
Sato, Y., Landisman, M., Ewing, M., 1960. Love waves in a heterogeneous spherical Earth. Journal of Geophysical Research 65, 5243–5255. https://doi.org/10.1029/jz067i013p05243
Schaeffer, A.J., Lebedev, S., 2015. Global heterogeneity of the lithosphere and underlying mantle : A seismological appraisal based on multimode surface-wave dispersion analysis , shear-velocity tomography , and tectonic regionalization, in: The Earth's Heterogeneous Mantle. Springer International Publishing, pp. 3–46.
Schaeffer, A.J., Lebedev, S., 2014. Imaging the North American continent using waveform inversion of global and USArray data. Earth and Planetary Science Letters 402, 26–41. https://doi.org/10.1016/j.epsl.2014.05.014
Schaeffer, A.J., Lebedev, S., 2013. Global shear speed structure of the upper mantle and transition zone. Geophysical Journal International 194, 417–449. https://doi.org/10.1093/gji/ggt095
Schaeffer, A.J., Lebedev, S., Becker, T.W., 2016. Azimuthal seismic anisotropy in the Earth's upper mantle and the thickness of tectonic plates. Geophysical Journal International 207, 901–933. https://doi.org/10.1093/gji/ggw309
Schlue, J.W., Knopoff, L., 1977. Shear-wave polarization anisotropy in the Pacific Basin. Geophysical Journal of the Royal Astronomical Society 49, 145–165. https://doi.org/10.1111/j.1365-246X.1977.tb03706.x
Shapiro, N.M., Ritzwoller, M.H., 2002. Monte-Carlo inversion for a global shear-velocity model of the crust and upper mantle. Geophysical Journal International 151, 88–105. https://doi.org/10.1046/j.1365-246X.2002.01742.x
Takeo, A., Kawakatsu, H., Isse, T., Nishida, K., Shiobara, H., Sugioka, H., Ito, A., Utada, H., 2018. In Situ Characterization of the Lithosphere-Asthenosphere System beneath NW Pacific Ocean Via Broadband Dispersion Survey With Two OBS Arrays. Geochemistry, Geophysics, Geosystems 19, 3529–3539. https://doi.org/10.1029/2018GC007588
Takeo, A., Nishida, K., Isse, T., Kawakatsu, H., Shiobara, H., Sugioka, H., Kanazawa, T., 2013. Radially anisotropic structure beneath the Shikoku Basin from broadband surface wave analysis of ocean bottom seismometer records. Journal of Geophysical Research: Solid Earth 118, 2878–2892. https://doi.org/10.1002/jgrb.50219
Team, T.M.S., 1998. Imaging the Deep Seismic Structure Beneath a Mid-Ocean Ridge: The MELT Experiment. Science 280, 1215–1218. https://doi.org/10.1126/science.280.5367.1215
Trampert, J., Van Heijst, H.J., 2002. Global azimuthal anisotropy in the transition zone. Science 296, 1297–1299. https://doi.org/10.1126/science.1070264
Trampert, J., Woodhouse, J.H., 1995. Global phase velocity maps of Love and Rayleigh waves between 40 and 150 seconds. Geophysical Journal International 122, 675–690. https://doi.org/10.1111/j.1365-246X.1995.tb07019.x
VanderBeek, B.P., Toomey, D.R., 2017. Shallow Mantle Anisotropy Beneath the Juan de Fuca Plate. Geophysical Research Letters 44, 11,382-11,389. https://doi.org/10.1002/2017GL074769

Visser, K., Trampert, J., Lebedev, S., Kennett, B.L.N., 2008. Probability of radial anisotropy in the deep mantle. Earth and Planetary Science Letters 270, 241–250. https://doi.org/10.1016/j.epsl.2008.03.041

Wang, Z., Dahlen, F.A., 1995. Spherical-spline parameterization of three-dimensional Earth models. Geophysical Research Letters 22, 3099–3102.

Wessel, P., Smith, W.H.F., Scharroo, R., Luis, J., Wobbe, F., 2013. Generic mapping tools: Improved version released. Eos 94, 409–410. https://doi.org/10.1002/2013EO450001

Wookey, J., Kendall, J.M., Barruol, G., 2002. Mid-mantle deformation inferred from seismic anisotropy. Nature 415, 777–780. https://doi.org/10.1038/415777a

Yang, X., Luo, Y., Xu, H., Zhao, K., 2020. Shear wave velocity and radial anisotropy structures beneath the central Pacific from surface wave analysis of OBS records. Earth and Planetary Science Letters 534, 116086. https://doi.org/10.1016/j.epsl.2020.116086

Yoshizawa, K., Kennett, B.L.N., 2002. Non-linear waveform inversion for surface waves with a neighbourhood algorithm-application to multimode dispersion measurements. Geophysical Journal International 149, 118–133. https://doi.org/10.1046/j.1365-246X.2002.01634.x

Yuan, K., Beghein, C., 2013. Seismic anisotropy changes across upper mantle phase transitions. Earth and Planetary Science Letters 374, 132–144. https://doi.org/10.1016/j.epsl.2013.05.031

Zhang, H., Maceira, M., Roux, P., Thurber, C., 2014. Joint Inversion of Body-Wave Arrival Times and Surface-Wave Dispersion for Three-Dimensional Seismic Structure Around SAFOD. Pure and Applied Geophysics 171, 3013–3022. https://doi.org/10.1007/s00024-014-0806-y

Zhang, X., Paulssen, H., Lebedev, S., Meier, T., 2009. 3D shear velocity structure beneath the Gulf of California from Rayleigh wave dispersion. Earth and Planetary Science Letters 279, 255–262. https://doi.org/10.1016/j.epsl.2009.01.003

Zhang, X., Paulssen, H., Lebedev, S., Meier, T., 2007. Surface wave tomography of the Gulf of California. Geophysical Research Letters 34, 1–5. https://doi.org/10.1029/2007GL030631

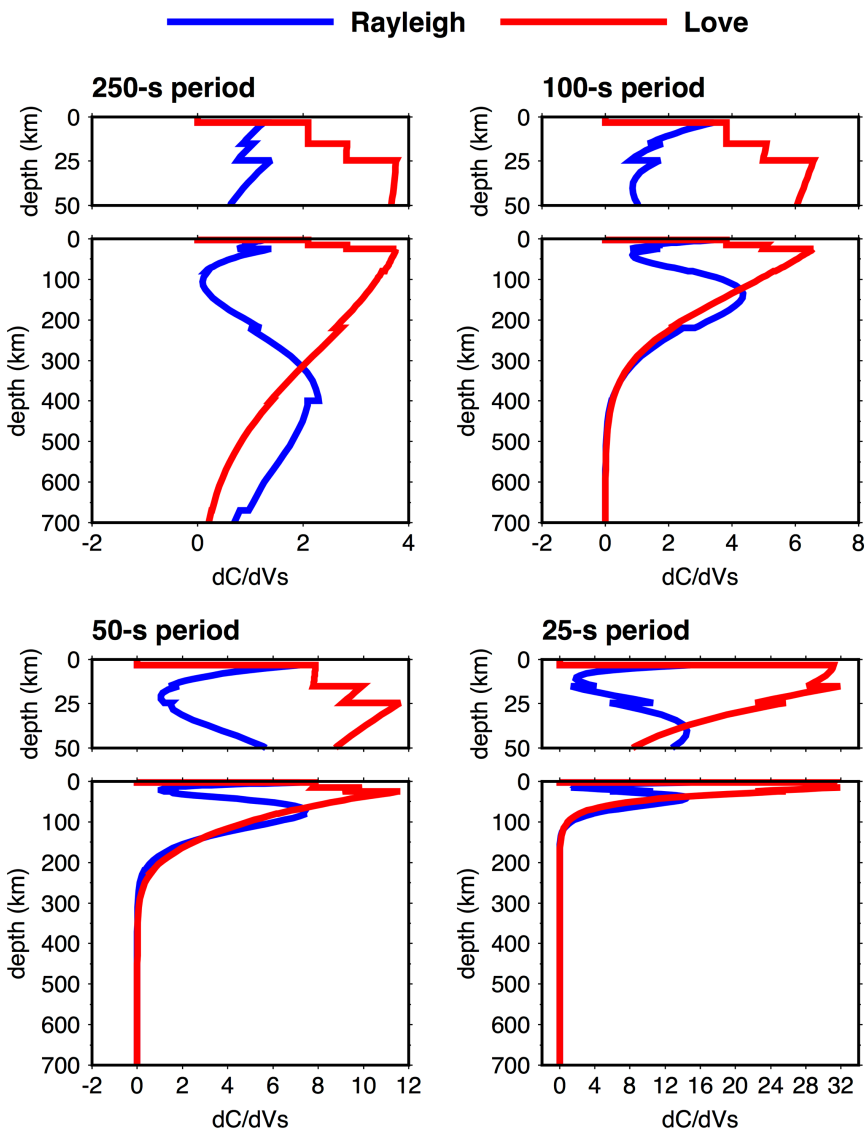

Figure 1. Depth sensitivity kernels of surface waves at four periods (25, 50, 150, and 250 s). The sensitivity curves are the Fréchet derivatives of the phase velocities of the fundamental-mode Rayleigh- (blue line) and Love- (red line) phase waves with respect to S-wave velocities at different depths. Note that the horizontal scale is different for each period.

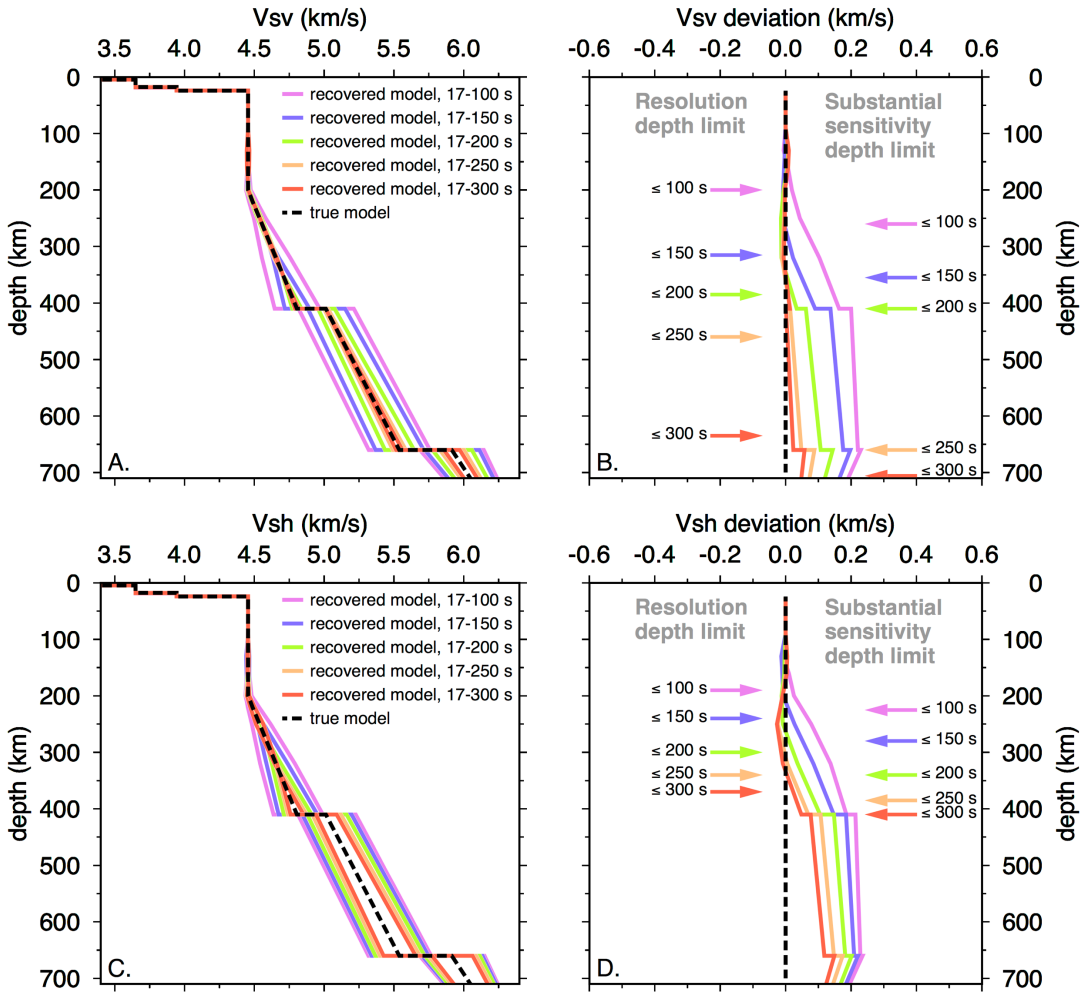

Figure 2. Sensitivity tests to estimate the maximum depth of the resolution given by surface waves with different long-period cutoffs: 100 s (violet line), 150 s (light blue line), 200 s (green line), 250 s (light orange line), and 300 s (red line). The panels on the left show the true V_S profile (dashed black line) and the ones given by inversions with *a priori* ± 250 m/s perturbations (coloured lines based on the cutoff of the synthetic dispersion curves). The panels on the right show the deviation of each profile from the true one. A-B) V_{SV} profiles; C-D) V_{SH} profiles. The arrows in the positive domain of panels B-D indicate the depths down to which there is substantial sensitivity (0.05 km/s threshold). The arrows in the negative domain indicate the depth limit of resolution (0.02 km/s threshold), which show where we have sufficient resolving power to map anomaly depth distributions and amplitudes accurately. Note that the V_{SV} is well resolved down to the bottom of the MTZ and uppermost lower mantle using 250-300 s dispersion measurements. V_{SH} and anisotropy are resolved accurately down to the top of the MTZ with the longest-period 300 s measurements.

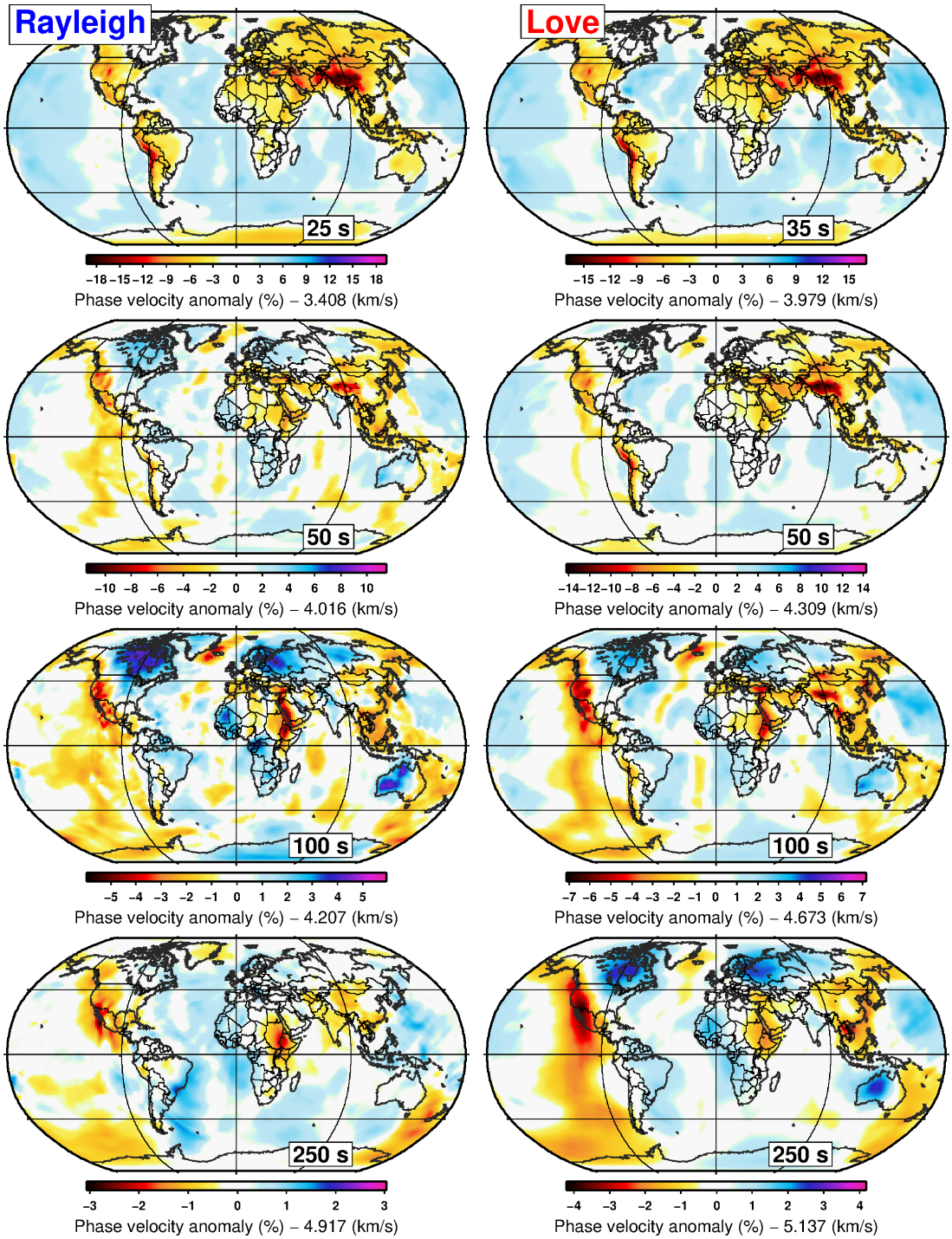

Figure 3. Phase velocity maps from 25 to 250 s for Rayleigh waves (left) and from 35 to 250 s for Love waves (right). The dispersion curves are from fundamental mode phase-velocity measurements performed on over 1.17 million vertical-component seismograms (for Rayleigh waves) and 300,000 transverse-component seismograms (Love waves) by the Automated Multimode Inversion (Lebedev et al., 2005).

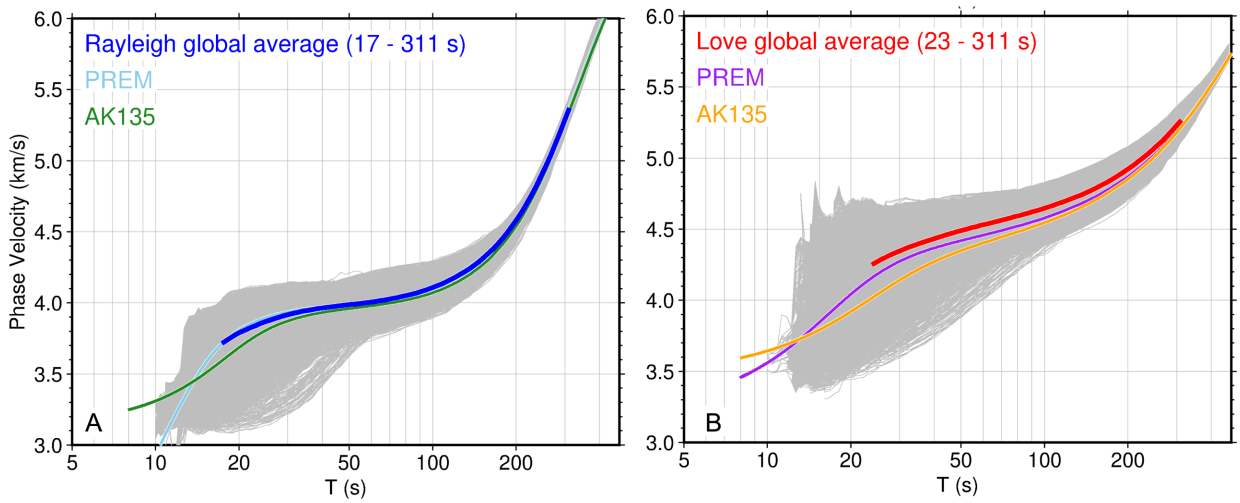

Figure 4. A. All the Rayleigh dispersion curves extracted from our phase-velocity maps (grey) and the global average curve (blue) in the period range 17-311 s. The Rayleigh-wave phase-velocity curves computed for PREM and AK135 are plotted in light blue and green, respectively. B. All the Love dispersion curves extracted from our phase-velocity maps (grey) and the global average curve (red) in the period range 23-311 s. The Love-wave phase-velocity curves computed for PREM and AK135 are plotted in purple and light orange, respectively. Note that the Love phase-velocity curve is substantially different from that given by PREM.

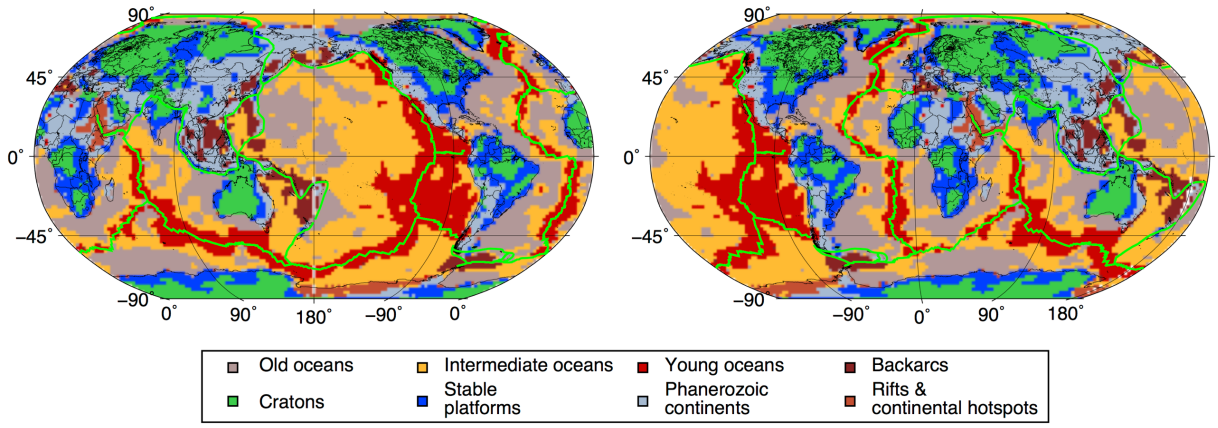

Figure 5. Tectonic regionalization of the Earth. The regionalization was computed from the model SL2013sv (Schaeffer and Lebedev, 2013) using *k*-means clustering of the tomography (Lekic and Romanowicz, 2011). The classification and colour of each region are given in the legend.

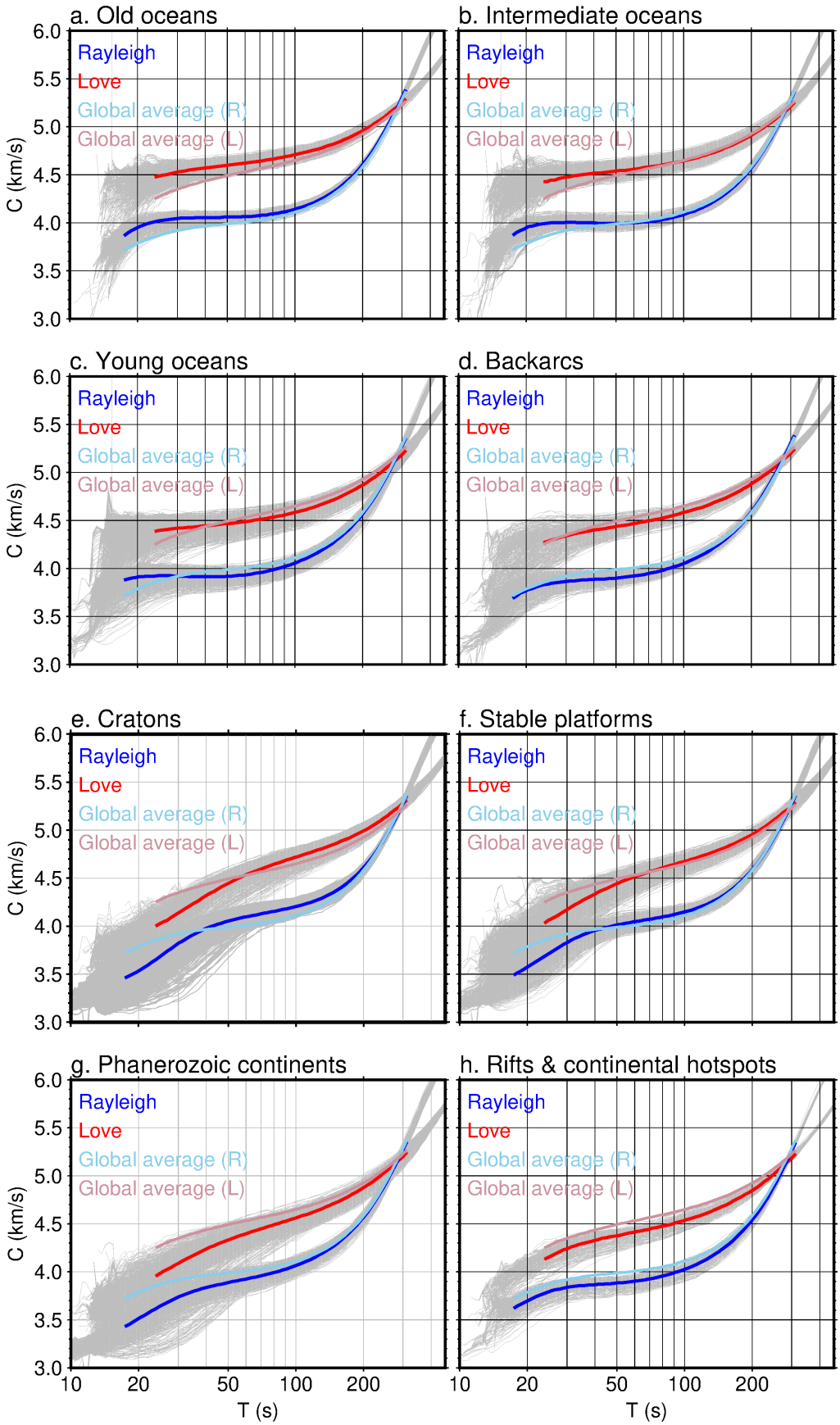

Figure 6. The tectonic-type dispersion curves extracted from the phase velocity maps at each knot of the 2°-spaced global grid for Rayleigh (blue) and Love (red) waves in the oceans: a) old oceans; b) intermediate oceans; c) young oceans; d) backarcs; and in the continents: e)

Archean cratons; f) stable platforms; g) Phanerozoic continents; h) rift zones and continental hotspots. For comparison, the Rayleigh and Love global average curves are plotted in each panel in light blue and light red, respectively.

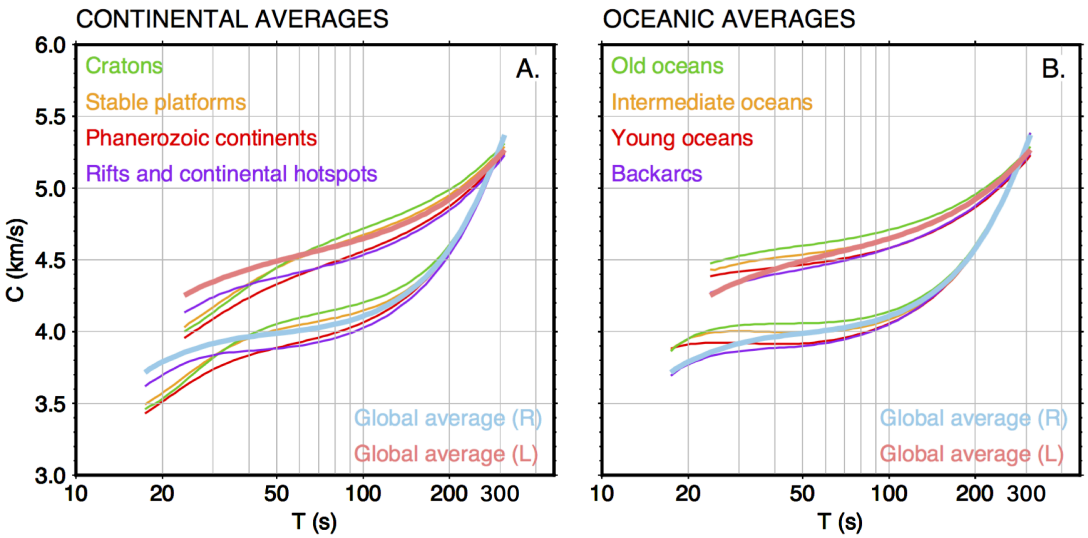

Figure 7. Average Rayleigh and Love phase-velocity curves in oceans (A) and continents (B). The Rayleigh and Love global average curves are plotted in both panels in light blue and light red, respectively.

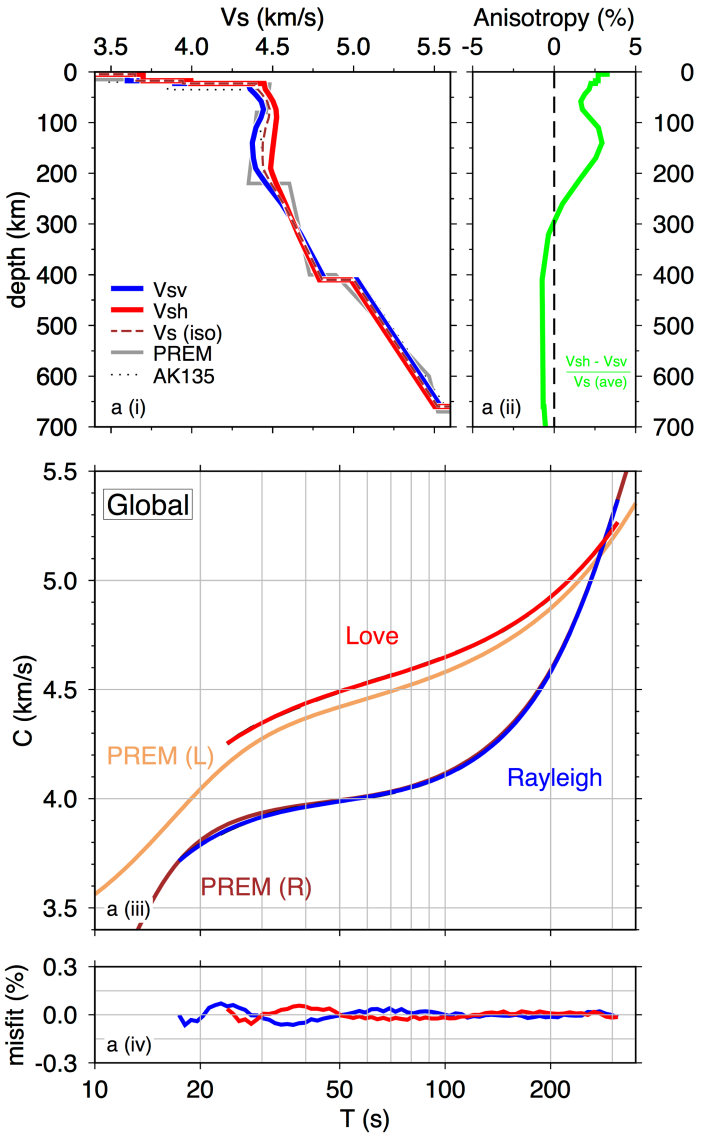

Figure 8. a (i) Example global-average V_{SV}, V_{SH} and isotropic V_S profiles (blue, red, dashed brown, respectively) in the crust and upper mantle yielded by the inversion of the surface-wave data. The isotropic-average AK135 and PREM models are plotted with a dotted black and thick gray lines, respectively. Here and in the following, all Vs models are computed or recomputed at a 50-s reference period. a (ii) Radial anisotropy. a (iii) The synthetic Rayleigh and Love phase-velocity curves (blue and red, respectively) and the measured curves (plotted behind them). The Rayleigh and Love PREM curves (Dziewonski et al., 1981) are shown in brown and orange, respectively. a (iv) The synthetic-data misfit in percent for the Rayleigh (blue) and Love curves (red).

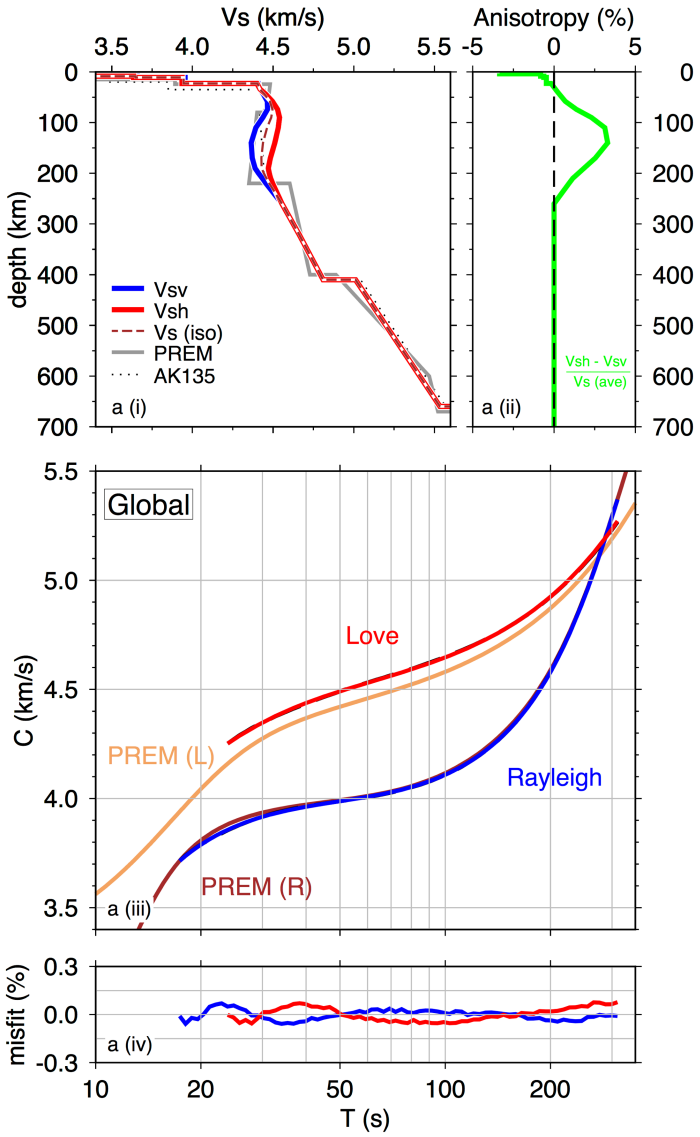

Figure 9. Test inversion showing that negative (V_{SV} > V_{SH}) radial anisotropy in the deep upper mantle is required by the data. In the gradient-search inversion, the anisotropy is forced to be null in the deep upper mantle (>250 km depth, see panels a(i-ii)), while anisotropy at shallower depths and isotropic V_S everywhere are allowed to vary freely. Note that the misfit deteriorates at long periods (T > 150 s) (see panels a(iii-iv)).

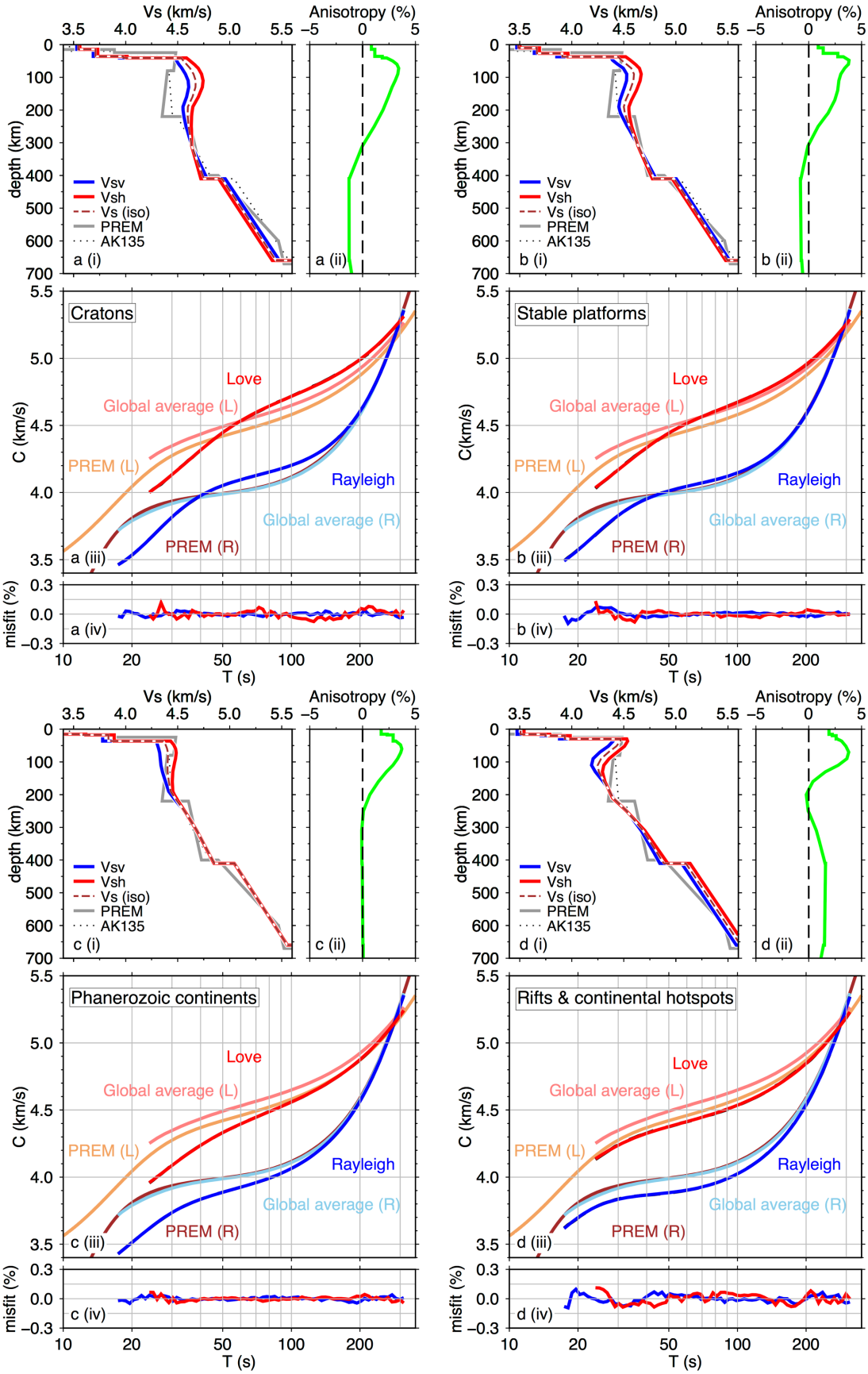

Figure 10. a-d(i) Example V_{SV} and V_{SH} profiles in the crust and upper mantle beneath continents yielded by the inversion of the surface-wave data: a(i) Archean cratons, b(i) stable platforms, c(i) Phanerozoic continents, and d(i) rifts and continental hotspots. a -d(ii) Radial

anisotropy for the 4 continental lithospheric types. The isotropic V_S is plotted with a dashed, brown line. The isotropic AK135 and PREM models are plotted with a dotted, black line and thick gray line, respectively. a-d(iii) The synthetic Rayleigh (dashed blue) and Love (dashed brown) phase-velocity curves and the measured curves (plotted behind), PREM curves (Dziewonski et al., 1981) (Rayleigh, light brown; Love, orange) and global averages (Rayleigh, light blue; Love, light red) are plotted for reference. a-d(iv) The synthetic-data misfit for Rayleigh (blue) and Love (brown) curves.

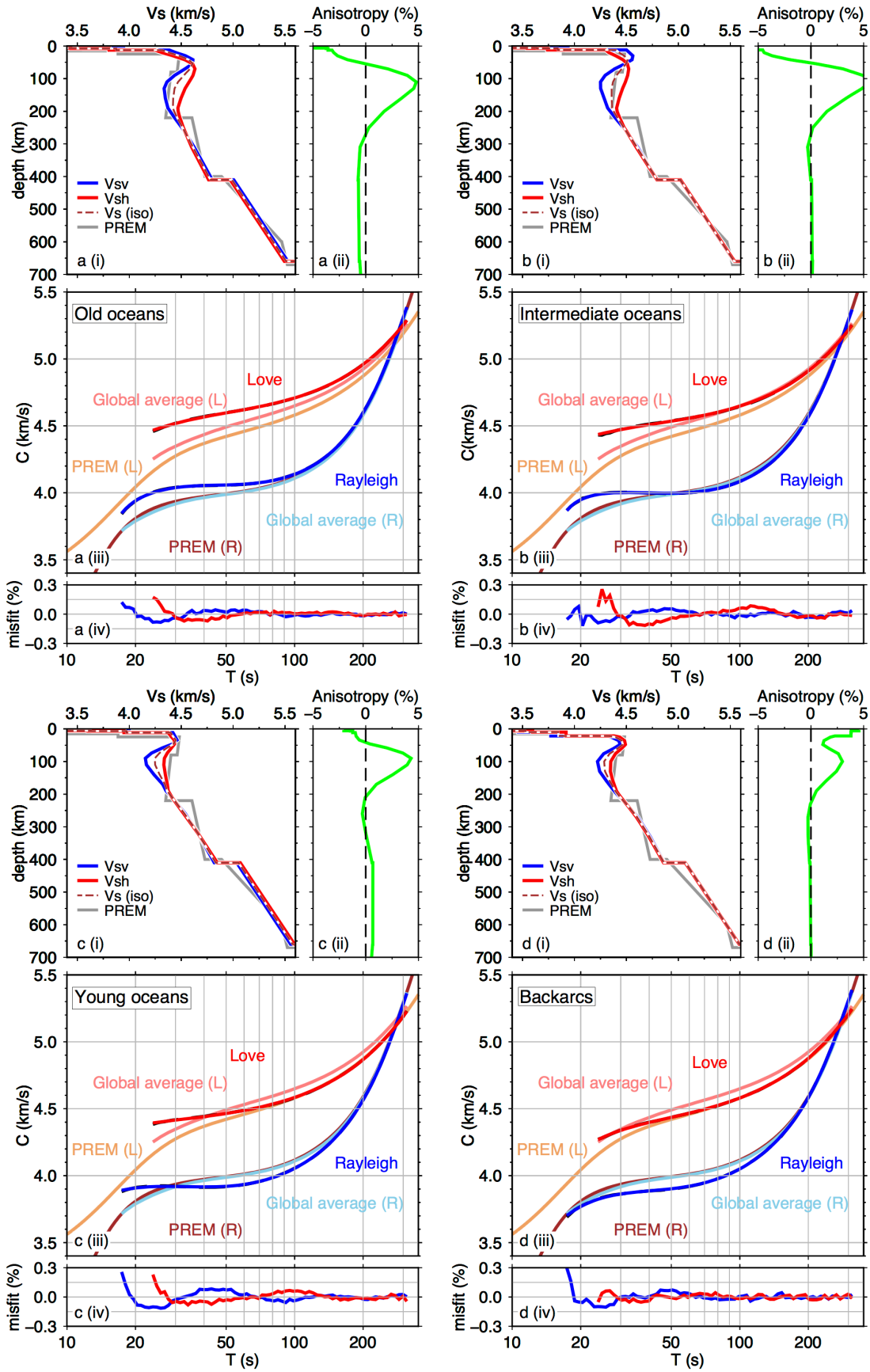

Figure 11. Same as Figure 10 but for oceans: a(i) old oceans, b(i) intermediate oceans, c(i) young oceans, and d(i) backarcs. PREM model is plotted with a thick grey line in panels a-d(i).

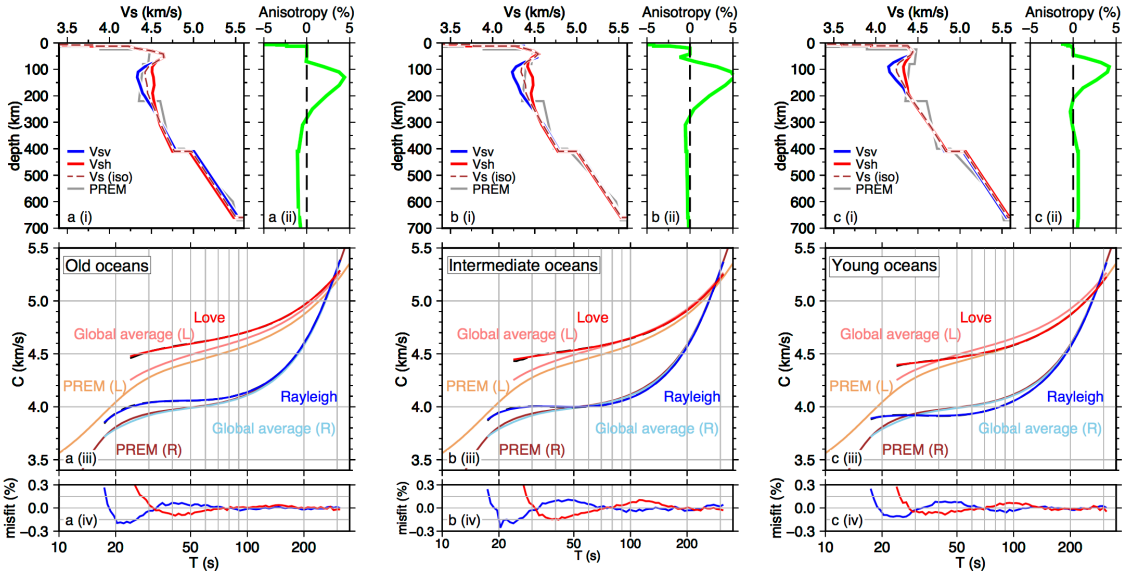

Figure 12. Test inversions showing that strong negative anisotropy ($V_{SV} > V_{SH}$) in the shallow mantle lithosphere is required by the data beneath: a(i) old oceans, b(i) intermediate oceans; and c(i) young oceans. If anisotropy is set to zero in the depth range from the Moho down to 50 km depth (panels a(ii), b(ii), and c(ii)), the fit deteriorates significantly at short and intermediate periods for all the oceanic clusters, even though all other inversion parameters can vary freely (see panels a(iii-iv), b(iii-iv), and c(iii-iv)). Our Rayleigh- (blue line) and Love-wave (red line) global average phase-velocity curves as well as the PREM (Rayleigh: light brown line; Love: orange) curves (Dziewonski et al., 1981) are plotted in panels a-c(iii) for comparison.

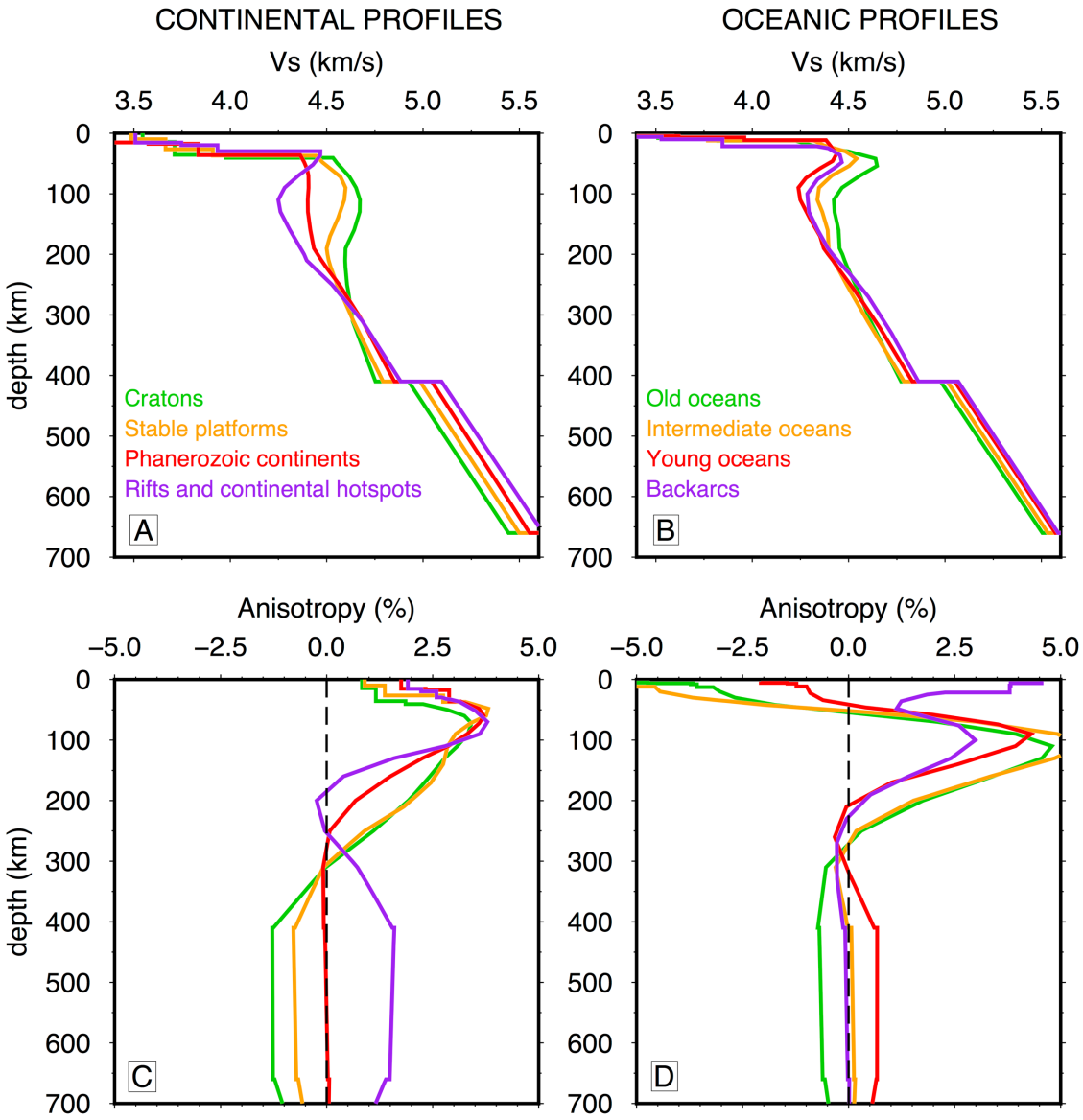

Figure 13. 1D isotropic V_S and anisotropy profiles for continents (A and C, respectively): cratons (green), stable platforms (orange), Phanerozoic continents (red), and rifts and continental hotspots (purple); and oceans (B and D, respectively): old oceans (green), intermediate oceans (orange), young oceans (red), and backarcs (purple). Note the overall age dependence of the lithospheric thickness (older lithosphere is thicker and colder) for both continents and oceans.

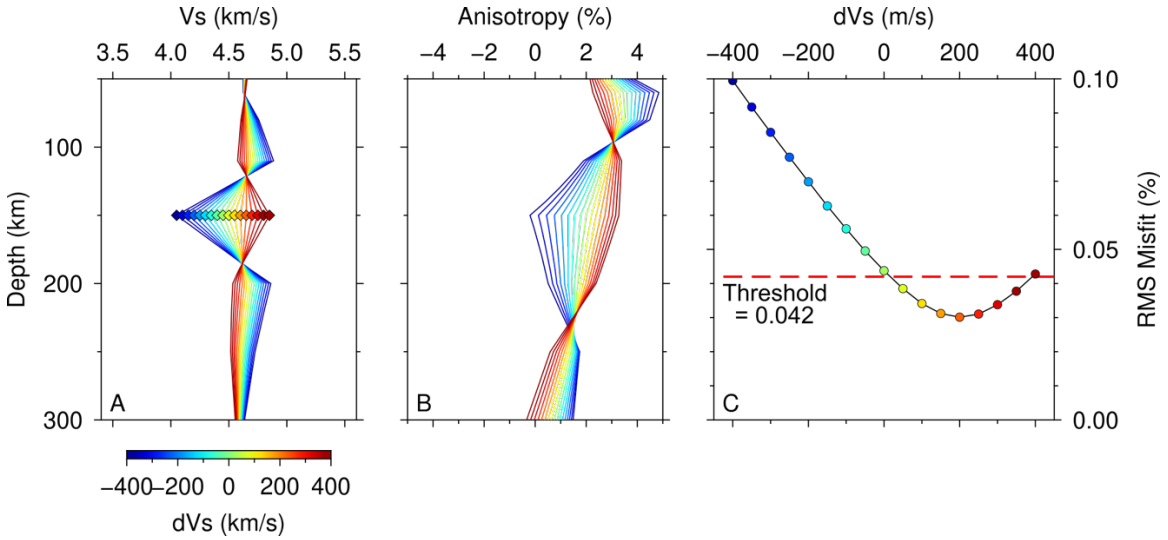

Figure 14. An illustration of the model-space-projection measurement of the uncertainty at a 150 km depth. The average dispersion curves of the cratons are used. (a) Isotropic Vs profiles produced by inversions with the Vs-perturbation parameter at the 150 km depths being fixed at values in the 4.1-4.9 km range, incremented at a 50 m/s interval. The rest of the parameters can change freely, subject to the same regularisation as in the optimal model (Figure 10a). The Vs profiles are color-coded by the Vs value at 150 km depth. (b) Anisotropy profiles produced by these inversions. (c) The RMS misfits of these inversions. The dots are color-coded in the same way as (a) and (b). The dashed red line marks the threshold below which the models are accepted.

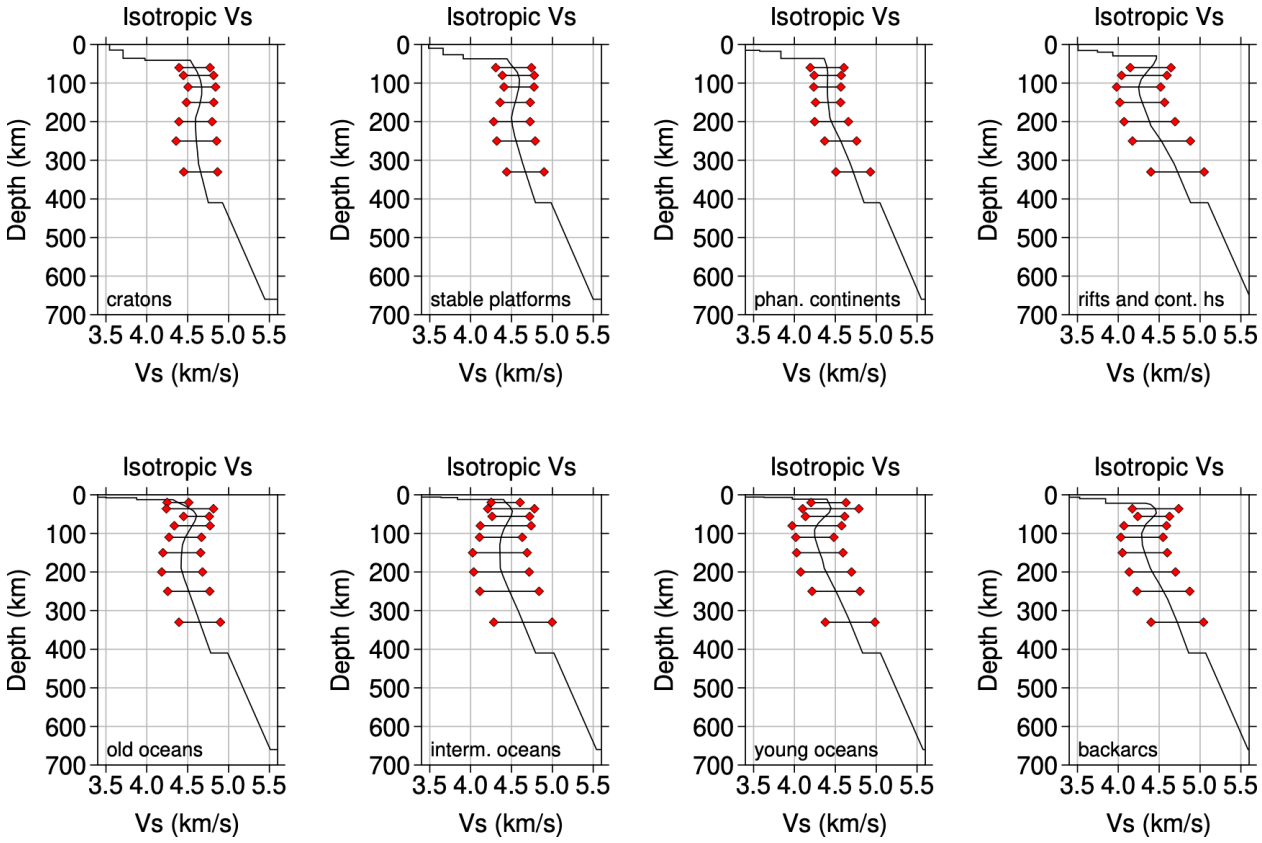

Figure 15. Uncertainties of the isotropic V_S models for the eight tectonic types computed using the model-space-projection technique for the radial parameter-knot spacing indicated by the depth intervals between the error bars. The horizontal lines (error bars) mark the range of velocity within which the misfit is below a specified threshold. The large uncertainties reflect the trade-offs of parameters at neighbouring depths and characterise the non-uniqueness of the small-scale components of the radial structure. Structure in broader depth ranges is constrained by the data with much smaller uncertainties (Figures 16-18).

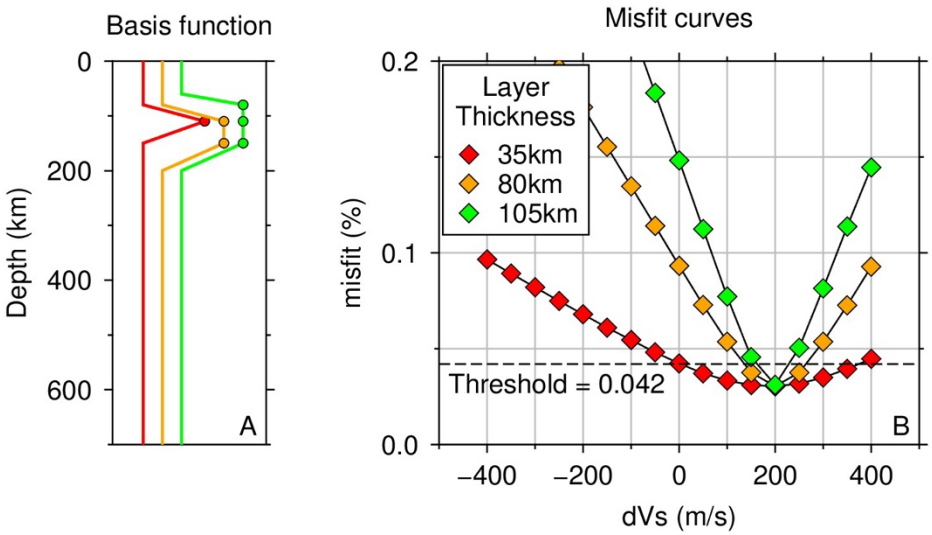

Figure 16. Dependence of the uncertainties of Vs within a layer on the thickness of the layer. (a) The definitions of the layers that are fixed during the inversions in this example. Three cases are shown: red – 1 basis function is fixed; orange – 2 basis function are fixed; green – 3 basis functions are fixed; (b) RMS misfits in the three cases. The layer thickness is computed using the full width at half height of the basis functions. Note how the green line (thickest layer) yields a smaller uncertainty range than the other two.

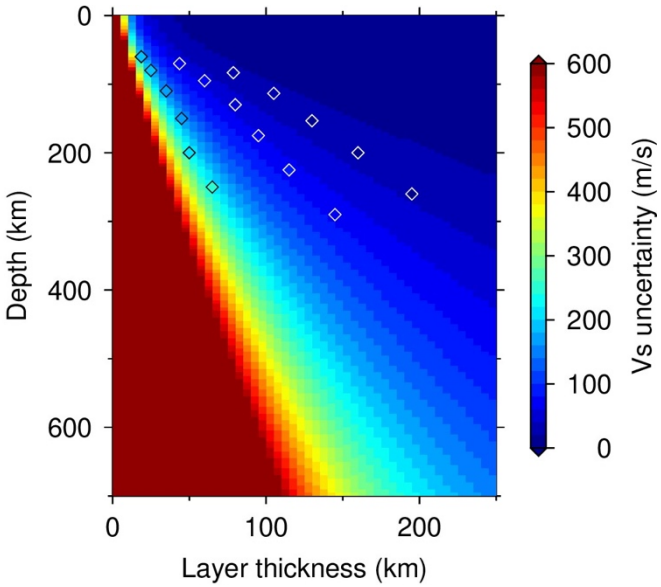

Figure 17. Uncertainty of Vs within a layer as a function of the depth and thickness of the layer. Each diamond indicates the layer depth and thickness values at which the uncertainty was calculated, as shown in Figure 16B. The background surface is the best fitting surface obtained using the Trust Region Reflective algorithm (Branch et al., 1999). This surface can be described as $U = (10984 + 8.40D^{1.87}) H^{-1.70}$, where U is the uncertainty in m/s, D is the depth in km, and H is the thickness in km.

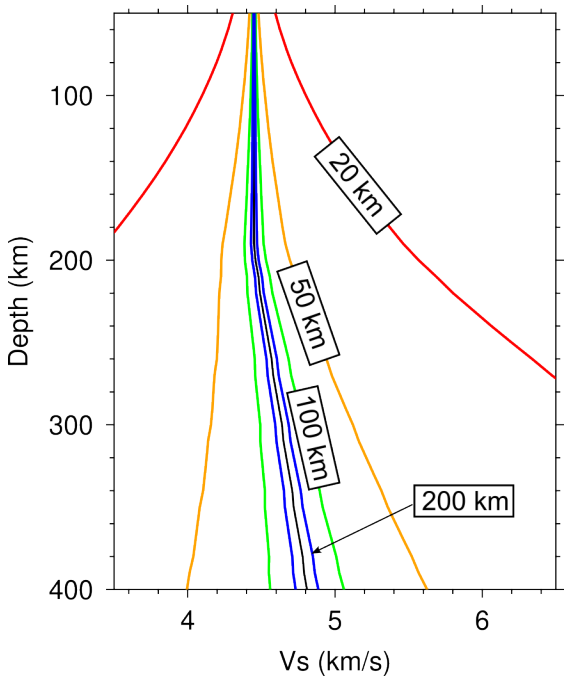

Figure 18. Uncertainties of the isotropic Vs profile of the cratons in the upper mantle. The black line in the centre is the isotropic Vs profile. The coloured lines show the uncertainties of Vs within a layer at a depth as a function of the thickness of the layer (20, 50, 100 or 200 km) and the depth.

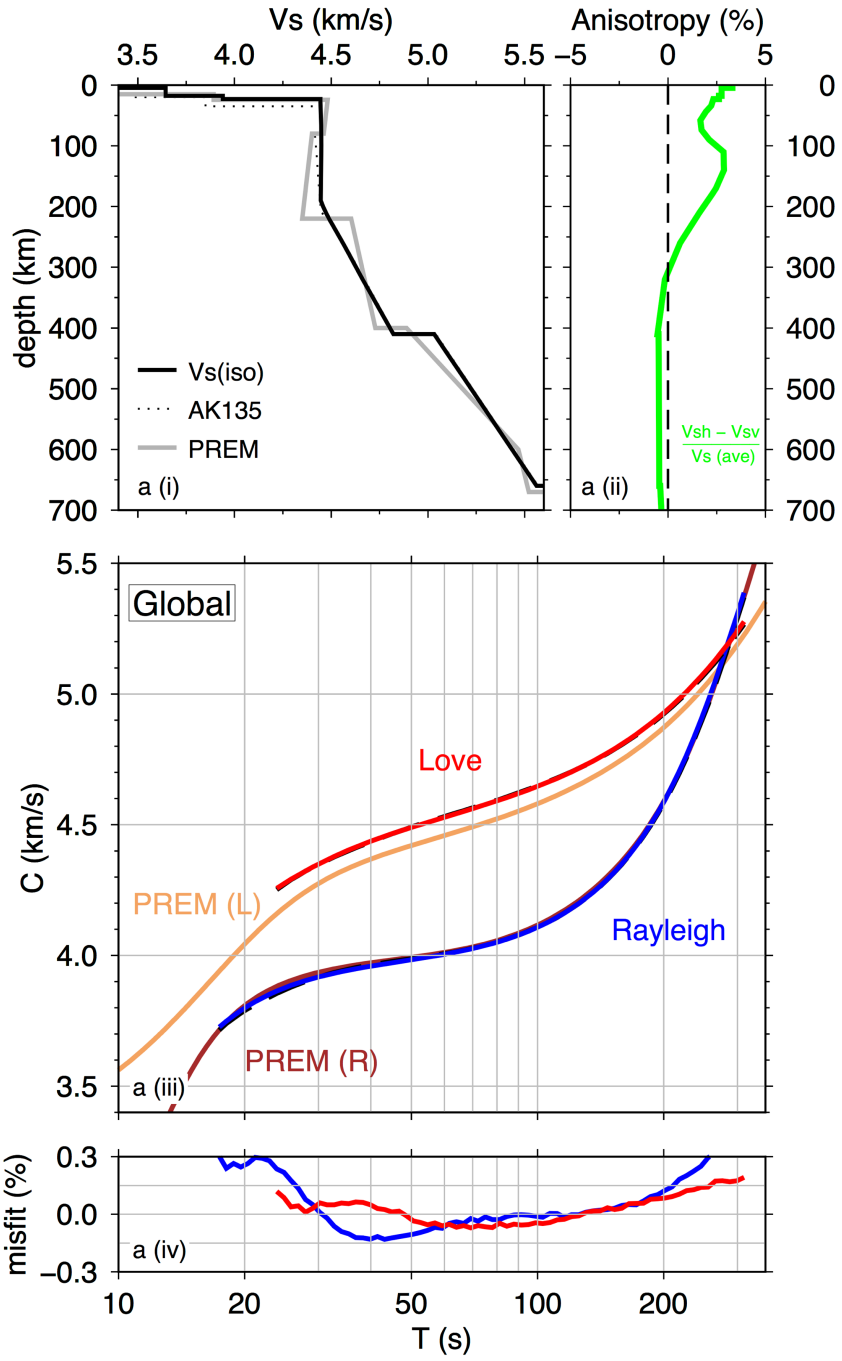

Figure 19. A simplified, AK135-like, global average model. The panels are the same as those in Figure 8. The isotropic AK135 and PREM models are plotted with a dotted, black line and thick gray line, respectively. All models are computed at a 50-s reference period. The best-fitting, minimum-complexity isotropic V_S profile (black line in panel a(i)) is similar to the AK135 model (dotted black line) and does not show any structural complexities in the upper mantle.

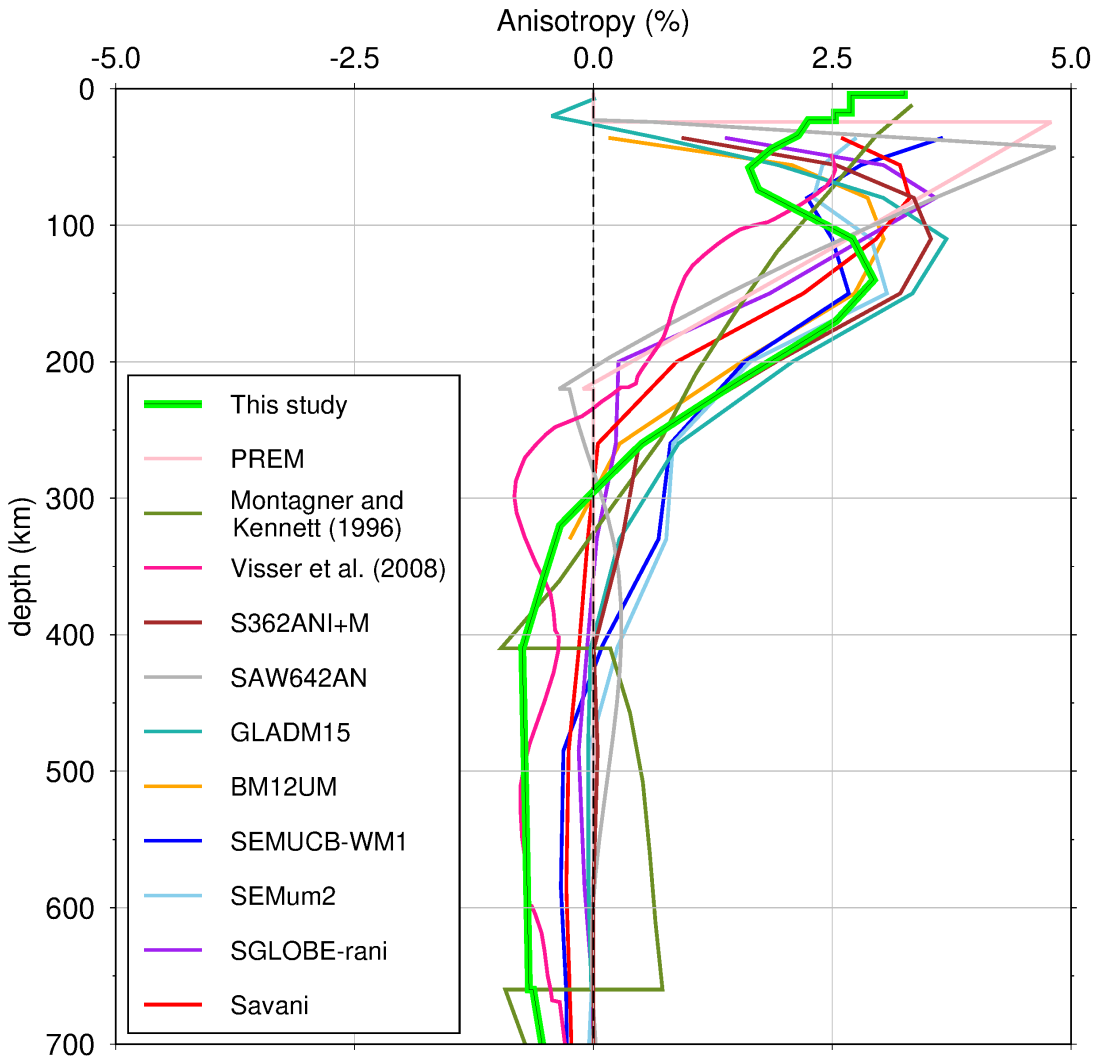

Figure 20. Comparison of 1D radially anisotropic profiles from Savani (Auer et al., 2014) (red line), SGLOBE-rani (Chang et al., 2015) (purple line), SEMum2 (French et al., 2013) (sky blue line), SEMUCB-WM1 (French and Romanowicz, 2014) (blue line), BM12UM (Burgos et al., 2014) (orange line), GLADM15 (Bozdağ et al., 2016) (sea green line), SAW642AN (Panning and Romanowicz, 2006) (gray line), S362ANI+M (Moulik and Ekström, 2014) (brown line), the model of (Visser et al., 2008) (deep pink line), that of (Montagner and Kennett, 1996) (olive green line, PREM (Dziewonski and Anderson, 1981) (pink line), and the anisotropic profile obtained in this study (thick green line). The anisotropy in the models of (Visser et al., 2008) and (Montagner and Kennett, 1996) is given as $xi=(V_{SH}/ V_{SV})^2$ and to derive anisotropy here we use $\sqrt{|xi|} -1$ assuming $V_{SH} \sim V_{SV}$. Note the flip of the sign of anisotropy from positive to negative at ~200-300 km depth in some profiles including that obtained in this study.

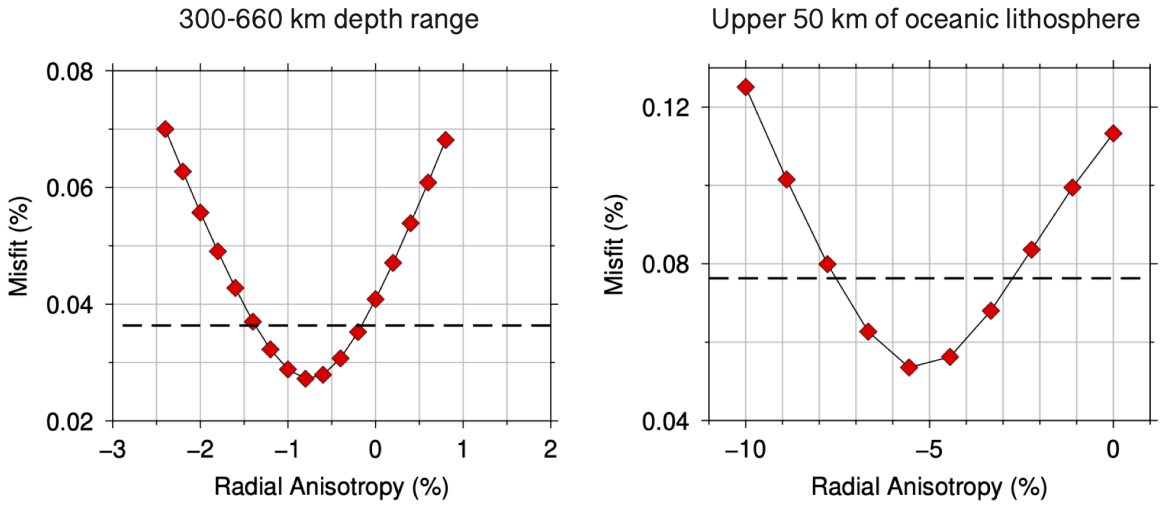

Figure 21. Model-space-projection measurements of the uncertainty of radial anisotropy in the 300-660 km depth range (left, 0.61% estimated uncertainty) and in the top 50 km of the lithosphere beneath intermediate oceans (right, 2.51% estimated uncertainty). The uncertainty is relatively small because it is for anisotropy in depth ranges that are sufficiently broad, at the depths.

References:

Auer, L., Boschi, L., Becker, T.W., Nissen-Meyer, T., Giardini, D., 2014. Savani: A variable resolution whole-mantle model of anisotropic shear velocity variations based on multiple data sets. Journal of Geophysical Research: Solid Earth 119, 3006–3034. https://doi.org/10.1002/2013JB010773

Bozdağ, E., Peter, D., Lefebvre, M., Komatitsch, D., Tromp, J., Hill, J., Podhorszki, N., Pugmire, D., 2016. Global adjoint tomography: First-generation model. Geophysical Journal International 207, 1739–1766. https://doi.org/10.1093/gji/ggw356

Branch, M.A., Coleman, T.F., Li, Y., 1999. A Subspace, Interior, and Conjugate Gradient Method for Large-Scale Bound-Constrained Minimization Problems. SIAM J. Sci. Comput. 21, 1–23. https://doi.org/10.1137/S1064827595289108

Burgos, G., Montagner, J., Beucler, E., Capdeville, Y., Mocquet, A., Drilleau, M., 2014. Oceanic lithosphere-asthenosphere boundary from surface wave dispersion data. Journal of Geophysical Research : Solid Earth 119, 1079–1093. https://doi.org/10.1002/2013JB010528.Abstract

Chang, S.J., Ferreira, A.M.G., Ritsema, J., Heijst, H.J., Woodhouse, J.H., 2015. Joint inversion for global isotropic and radially anisotropic mantle structure including crustal thickness perturbations. Journal of Geophysical Research : Solid Earth 120, 4278–4300. https://doi.org/10.1002/2014JB011824.Received

Dziewonski, A.M., Anderson, D.L., 1981. Preliminary reference Earth model. Physics of the Earth and Planetary Interiors 25, 297–356. https://doi.org/10.1016/0031-9201(81)90046-7

Dziewonski, A.M., Chou, T.A., Woodhouse, J.H., 1981. Determination of earthquake source parameters from waveform data for studies of global and regional seismicity. Journal of Geophysical Research 86, 2825–2852. https://doi.org/10.1029/JB086iB04p02825

French, S., Lekic, V., Romanowicz, B., 2013. Waveform tomography reveals channeled flow at the base of the oceanic asthenosphere. Science 342, 227–230. https://doi.org/10.1126/science.1241514

French, S.W., Romanowicz, B.A., 2014. Whole-mantle radially anisotropic shear velocity structure from spectral-element waveform tomography. Geophysical Journal International 199, 1303–1327. https://doi.org/10.1093/gji/ggu334

Lebedev, S., Nolet, G., Meier, T., van der Hilst, R.D., 2005. Automated multimode inversion of surface and S waveforms. Geophysical Journal International 162, 951–964. https://doi.org/10.1111/j.1365-246X.2005.02708.x

Lekic, V., Romanowicz, B., 2011. Tectonic regionalization without a priori information: A cluster analysis of upper mantle tomography. Earth and Planetary Science Letters 308, 151–160. https://doi.org/10.1016/j.epsl.2011.05.050

Montagner, J.P., Kennett, B.L.N., 1996. How to reconcile body-wave and normal-mode reference earth models. Geophysical Journal International 125, 229–248. https://doi.org/10.1111/j.1365-246X.1996.tb06548.x

Moulik, P., Ekström, G., 2014. An anisotropic shear velocity model of the Earth's mantle using normal modes, body waves, surface waves and long-period waveforms. Geophysical Journal International 199, 1713–1738. https://doi.org/10.1093/gji/ggu356

Panning, M., Romanowicz, B., 2006. A three-dimensional radially anisotropic model of shear velocity in the whole mantle. Geophysical Journal International 167, 361–379. https://doi.org/10.1111/j.1365-246X.2006.03100.x

Schaeffer, A.J., Lebedev, S., 2013. Global shear speed structure of the upper mantle and transition zone. Geophysical Journal International 194, 417–449. https://doi.org/10.1093/gji/ggt095

Visser, K., Trampert, J., Lebedev, S., Kennett, B.L.N., 2008. Probability of radial anisotropy in the deep mantle. Earth and Planetary Science Letters 270, 241–250. https://doi.org/10.1016/j.epsl.2008.03.041

Supplemental Material

Toward tectonic-type and global 1D seismic models of the upper mantle constrained by broadband surface waves

Chiara Civiero[*1,2], Sergei Lebedev[2,3], Yihe Xu[2,3], Raffaele Bonadio[2,3], François Lavoué[2,4,5]

1) Department of Mathematics, Informatics and Geosciences, University of Trieste, Italy
2) Dublin Institute for Advanced Studies (DIAS), Dublin D02 Y006, Ireland
3) Bullard Laboratories, Department of Earth Sciences, University of Cambridge, Cambridge CB30EZ, UK
4) Institut de Radioprotection et Sûreté Nucléaire (IRSN), PSE-ENV, SCAN, BERSSIN, Fontenay-aux-Roses, France
5) Université Grenoble Alpes, Univ. Savoie Mont Blanc, CNRS, IRD, UGE, ISTerre, Grenoble, France

List of supplementary contents

This supplementary document includes 6 figures and 2 tables, all of which are referenced in the main document.

1. Table T1
2. Figure S1.
3. Figure S2.
4. Table T2
5. Figure S3.
6. Figure S4.
7. Figure S5.
8. Figure S6.

PARAMETERS	VALUES
DEPTH WATER LAYER (km)	-1.892
DEPTH SEDIMENTS (km)	-3.271
DEPTH UPPER CRUST (km)	-8.988
DEPTH MIDDLE CRUST (km)	-15.138
DEPTH LOWER CRUST (km)	-22.903
V_S WATER LAYER (m/s)	0
V_S SEDIMENTS (m/s)	800
V_S UPPER CRUST (m/s)	3070.67
V_S MIDDLE CRUST (m/s)	3698.73
V_S LOWER CRUST (m/s)	3997
V_P WATER LAYER (m/s)	1500
V_P SEDIMENTS (m/s)	1800
V_P UPPER CRUST (m/s)	5476.99
V_P MIDDLE CRUST (m/s)	6462.61
V_P LOWER CRUST (m/s)	7025.09
ρ WATER LAYER (kg/m^3)	1020
ρ SEDIMENTS (kg/m^3)	1800
ρ UPPER CRUST (kg/m^3)	2627.82
ρ MIDDLE CRUST (kg/m^3)	2829.66
ρ LOWER CRUST (kg/m^3)	3001.67

Table T1. Average global values of each crustal layer depth (in km), V_S, V_P, (in m/s), and density (ρ, in kg/m^3) from the CRUST1.0 model (Laske et al., 2013).

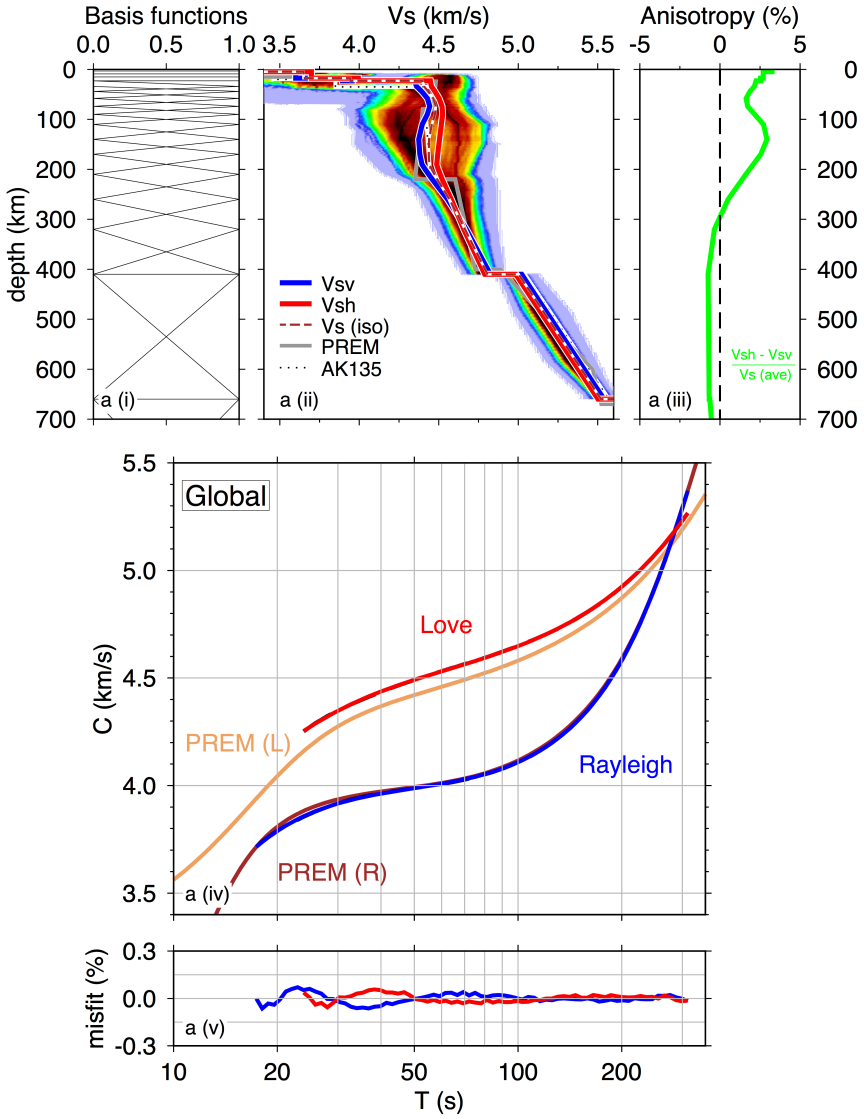

Figure S1. Same as Figure 8, but with the density of the 1D shear-speed profiles extracted from the global tomographic model SL2013sv of Schaeffer & Lebedev (2013) plotted behind the global average V_S model. The relative density of profiles at each depth and each shear-speed value is shown by colour, with blue tone colours indicating minimal sampling and warmer colours through to black indicating increasing sampling. The minimum/maximum velocity envelope is indicated by the light-blue shading. The basis functions are also included in panel a(i).

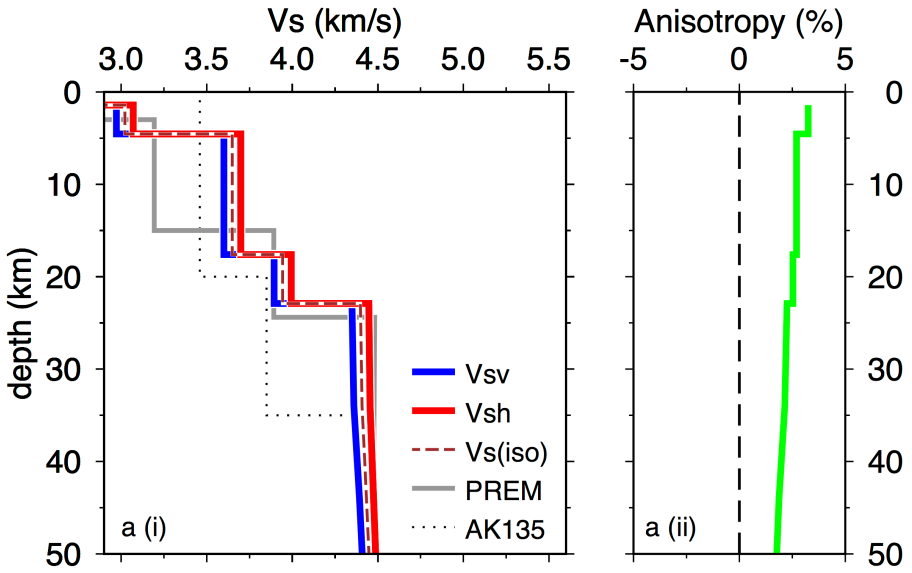

1571
1572
1573 Figure S2. Same as Figure 8, showing V_S and radial anisotropy with a zoom on the top
1574 50 km.

	CRATONS	STABLE PLATFORMS	PHAN. CONTINENTS	RIFTS & CONT. HOTSPOTS	YOUNG OCEANS	INTERM. OCEANS	OLD OCEANS	BACKARCS
DEPTH WATER LAYER (km)	/	/	/	/	-3.36	-4.47	-4.59	-2.59
DEPTH UPPER CRUST (km)	-13.72	-13.75	-13.67	-10.82	-4.56	-5.72	-6.22	-6.07
DEPTH MIDDLE CRUST (km)	-26.59	-26.05	-25.70	-20.01	-6.33	-7.25	-7.75	-9.48
DEPTH LOWER CRUST (km)	-37.23	-37.08	-36.46	-29.66	-11.40	-11.98	-12.47	-16.49
V_S WATER LAYER (m/s)	/	/	/	/	0	0	0	0
V_S UPPER CRUST (m/s)	3511.38	3528.48	3519.17	3549.53	2711.62	2700.13	2762.7	2910.74
V_S MIDDLE CRUST (m/s)	3665.16	3694.71	3709.77	3762.26	3690.81	3698.3	3703.75	3713.69
V_S LOWER CRUST (m/s)	3915.14	3939.07	3944.64	3924.5	4033.53	4049.12	4044.71	4019.51
V_P WATER LAYER (m/s)	/	/	/	/	1500	1500	1500	1500
V_P UPPER CRUST (m/s)	6053.84	6085.92	6063.03	6124.37	5005.64	5000.11	5069.86	5258.23
V_P MIDDLE CRUST (m/s)	6371.24	6421.6	6433.38	6527.99	6479.61	6494.91	6499.77	6502.95
V_P LOWER CRUST (m/s)	6866.57	6931.69	6955.94	7028.93	7075.22	7098.25	7099.4	7084.39
ρ WATER LAYER (kg/m^3)	/	/	/	/	1020	1020	1020	1020
ρ UPPER CRUST (kg/m^3)	2724.02	2728.03	2724.57	2759.4	2550	2549.96	2550	2587.85
ρ MIDDLE CRUST (kg/m^3)	2795.85	2803.32	2807.64	2848.9	2839.77	2848.69	2850	2842.36
ρ LOWER CRUST (kg/m^3)	2918	2937.64	2950.03	2998.52	3037.96	3049.1	3050	3035.13

Table T2. Average values of crustal layer depth (in km), V_S, V_P, (in m/s), and density (ρ in kg/m^3) from the CRUST1.0 model (Laske et al., 2013) for the eight tectonic environments across the globe.

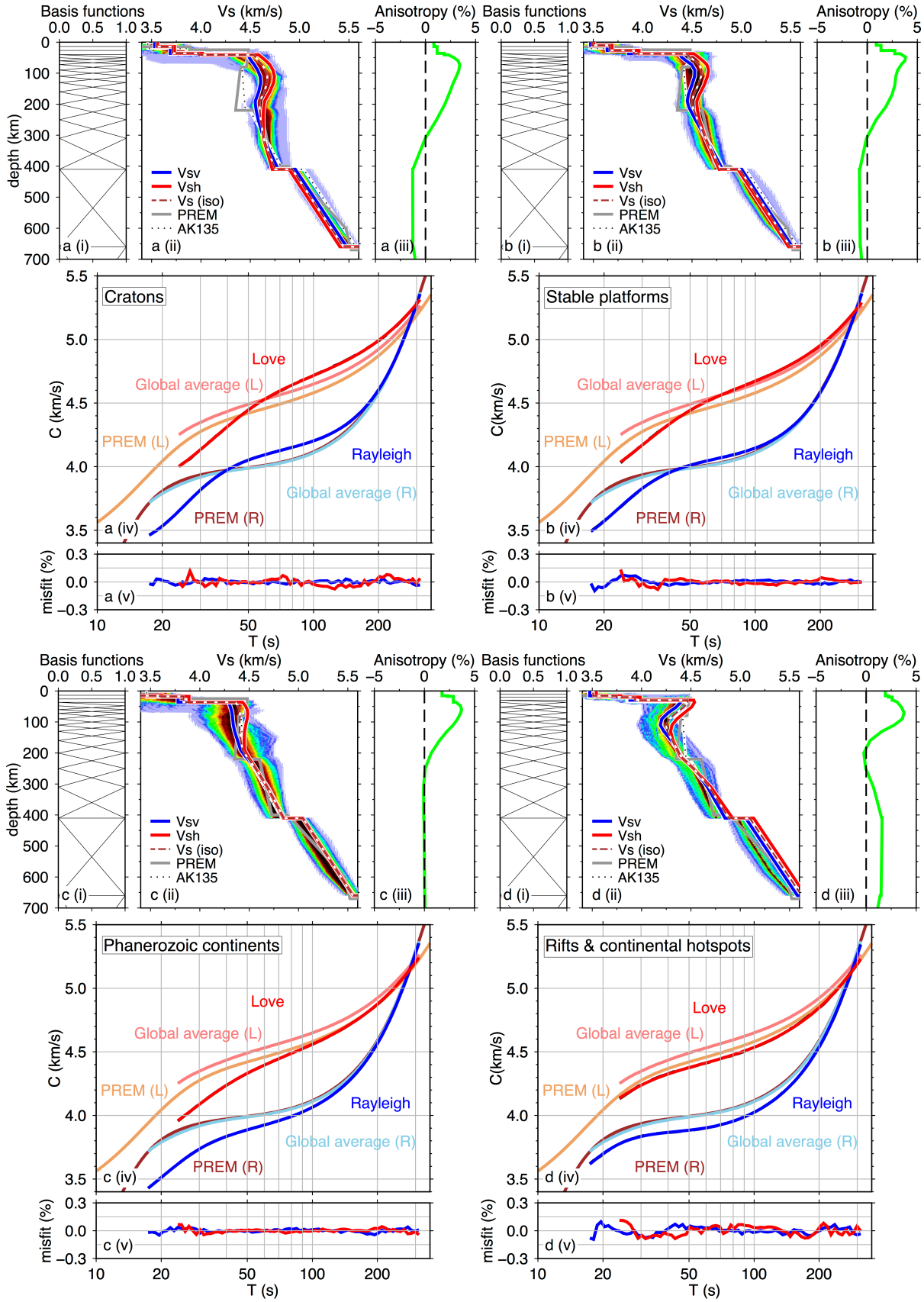

Figure S3. Same as Figure 10, but with the density of the 1D shear-speed profiles extracted from the global tomographic model SL2013sv of Schaeffer & Lebedev (2013) plotted together with our V_S models for each cluster. The relative density of profiles at each depth and each shear-speed value is shown by colour, with blue-tone colours indicating minimal

1585 sampling and warmer colours through to black indicating increasing sampling. The
1586 minimum/maximum velocity envelope is indicated by the light-blue shading. The basis
1587 functions are included in panels a-d(i).
1588

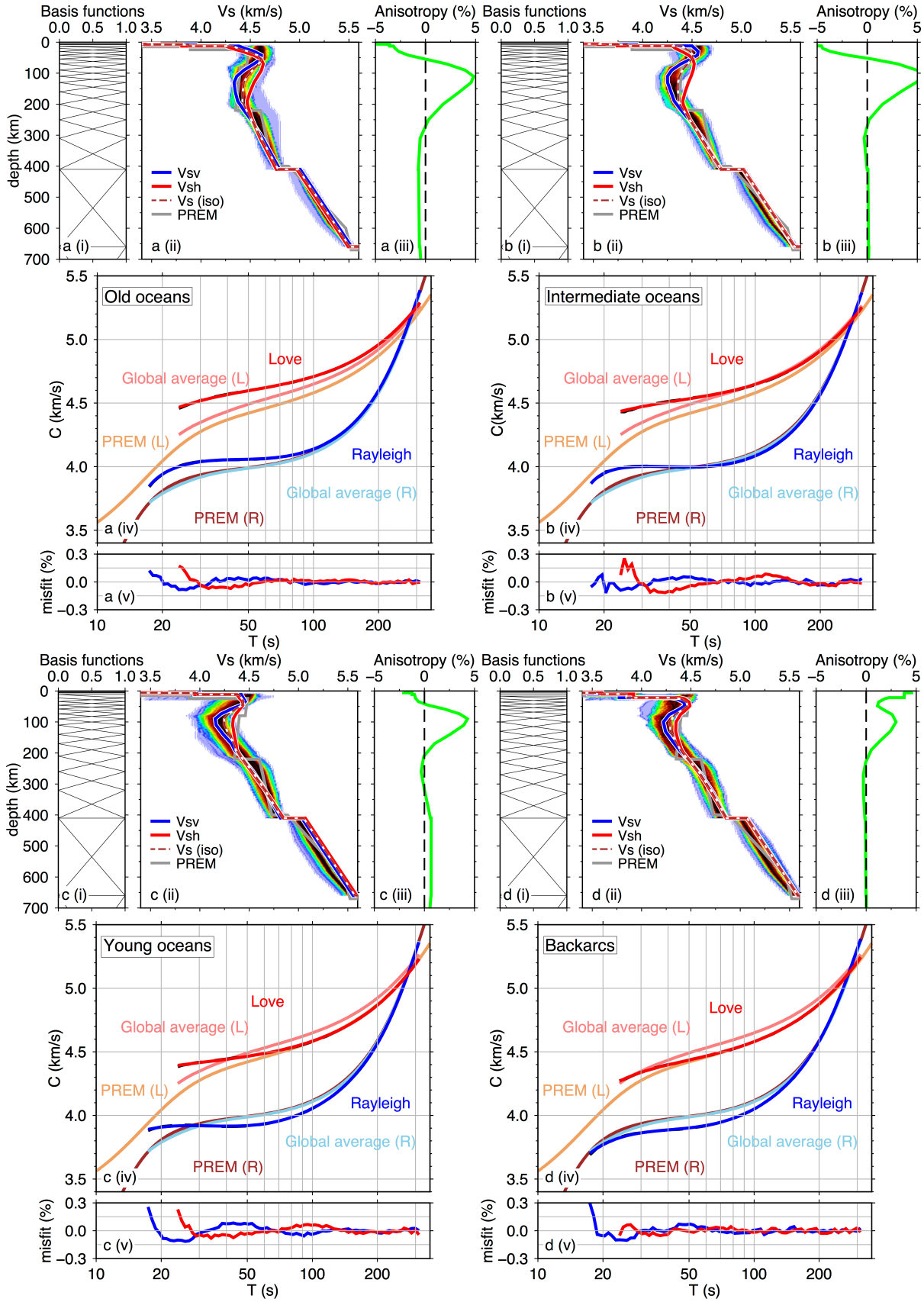

Figure S4. Same as Figure 11 (oceanic lithospheric types), but with the density of the 1D shear-speed profiles extracted from the global tomographic model SL2013sv of Schaeffer & Lebedev 2013) plotted together with our Vs models for each cluster. The basis functions are included in panels a-d(i).

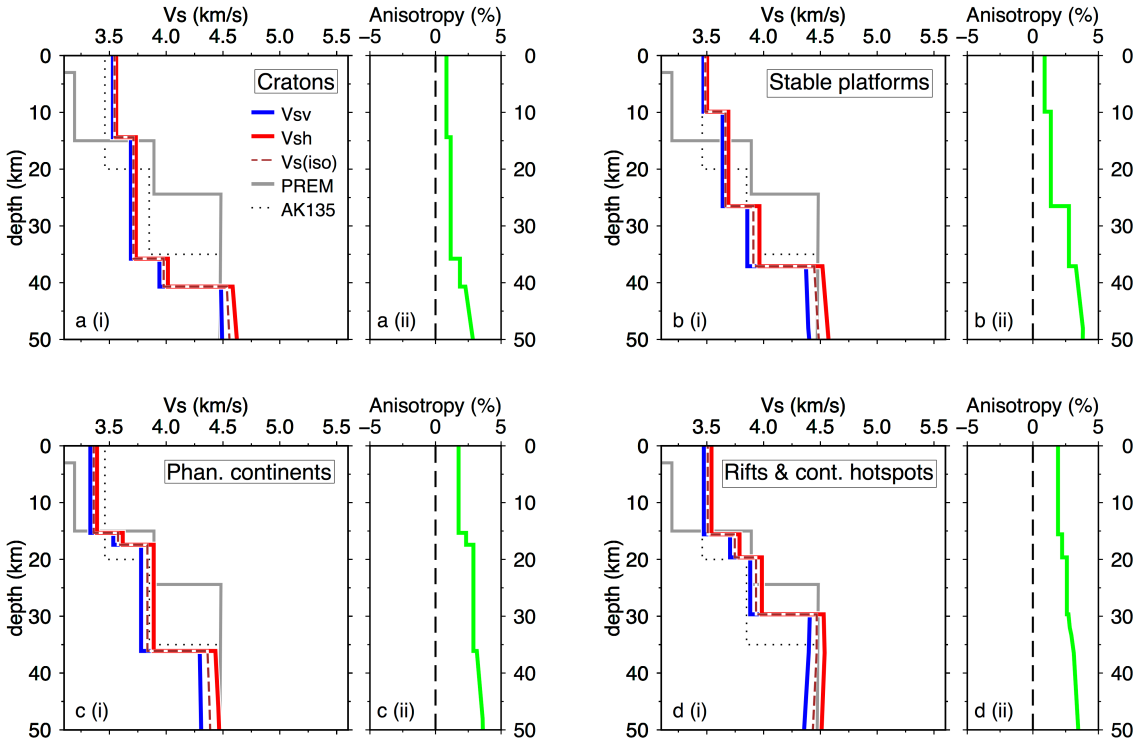

Figure S5. Same as Figure 10, showing V_S and radial anisotropy for each continental tectonic type, but with a zoom on the top 50 km below the surface. The isotropic AK135 and PREM models are plotted with a dotted, black line and thick gray line, respectively.

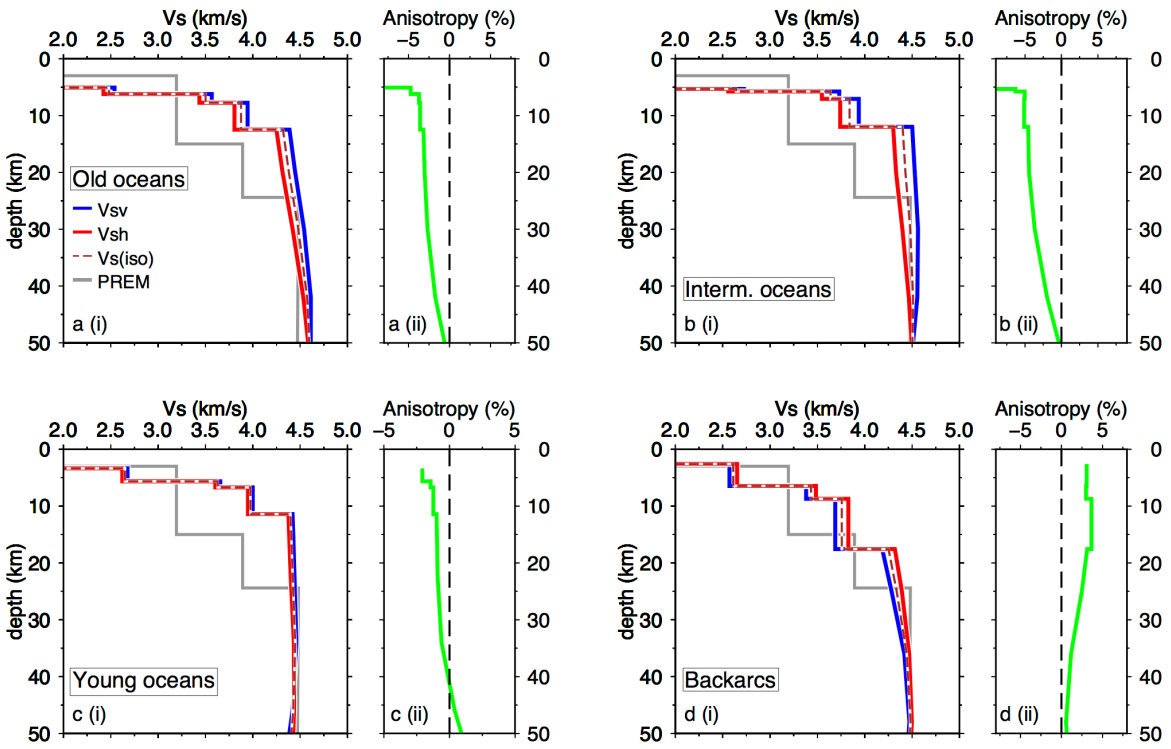

Figure S6. Same as Figure 11, showing V_S and radial anisotropy for each oceanic tectonic type, but with a zoom on the top 50 km. The PREM model is plotted with a thick gray line.